HHS Public Access

Author manuscript

Nature. Author manuscript; available in PMC 2024 February 26.

Published in final edited form as:

Nature. 2023 July ; 619(7969): 410–419. doi:10.1038/s41586-023-06175-5.

EMC chaperone–Ca_V structure reveals an ion channel assembly intermediate

Zhou Chen[1], **Abhisek Mondal**[1], **Fayal Abderemane-Ali**[1,8], **Seil Jang**[1], **Sangeeta Niranjan**[1], **José L. Montaño**[2], **Balyn W. Zaro**[1,2], **Daniel L. Minor Jr**[1,3,4,5,6,7,✉]

[1]Cardiovascular Research Institute, University of California, San Francisco, CA, USA.

[2]Department of Pharmaceutical Chemistry, University of California, San Francisco, CA, USA.

[3]Department of Biochemistry and Biophysics, University of California, San Francisco, CA, USA.

[4]California Institute for Quantitative Biomedical Research, University of California, San Francisco, CA, USA.

[5]Kavli Institute for Fundamental Neuroscience, University of California, San Francisco, CA, USA.

[6]Molecular Biophysics and Integrated Bio-imaging Division, Lawrence Berkeley National Laboratory, Berkeley, CA, USA.

[7]Department of Cellular and Molecular Pharmacology, University of California, San Francisco, CA, USA.

[8]Present address: Department of Physiology, David Geffen School of Medicine at UCLA, Los Angeles, CA, USA.

Abstract

Voltage-gated ion channels (VGICs) comprise multiple structural units, the assembly of which is required for function[1,2]. Structural understanding of how VGIC subunits assemble and whether chaperone proteins are required is lacking. High-voltage-activated calcium channels (Ca_Vs)[3,4] are paradigmatic multisubunit VGICs whose function and trafficking are powerfully shaped by interactions between pore-forming Ca_V1 or Ca_V2 $Ca_V\alpha_1$ (ref. 3), and the auxiliary $Ca_V\beta$[5] and $Ca_V\alpha_2\delta$ subunits[6,7]. Here we present cryo-electron microscopy structures of human brain and

✉ **Correspondence and requests for materials** should be addressed to Daniel L. Minor. daniel.minor@ucsf.edu.

Author contributions Z.C. and D.L.M. conceived the study and designed the experiments. Z.C. and S.N. expressed and characterized the samples. Z.C., A.M. and F.A.-A. collected and analysed cryo-EM data. Z.C. and A.M. built and refined the atomic models. Z.C. collected and analysed the two-electrode voltage clamp data. F.A.-A. and S.J. collected and analysed the whole-cell electrophysiology data. J.L.M. and B.W.Z. collected and analysed the MS data. B.W.Z. and D.L.M. analysed data and provided guidance and support. Z.C., A.M., F.A.-A., J.L.M., B.W.Z. and D.L.M. wrote the paper.

Competing interests The authors declare no competing interests.

Reporting summary

Further information on research design is available in the Nature Portfolio Reporting Summary linked to this article.

Additional information

Supplementary information The online version contains supplementary material available at https://doi.org/10.1038/s41586-023-06175-5.

Peer review information *Nature* thanks the anonymous reviewers for their contribution to the peer review of this work. Peer reviewer reports are available.

cardiac $Ca_V1.2$ bound with $Ca_V\beta_3$ to a chaperone—the endoplasmic reticulum membrane protein complex (EMC)[8,9]—and of the assembled $Ca_V1.2$–$Ca_V\beta_3$–$Ca_V\alpha_2\delta$-1 channel. These structures provide a view of an EMC–client complex and define EMC sites—the transmembrane (TM) and cytoplasmic (Cyto) docks; interaction between these sites and the client channel causes partial extraction of a pore subunit and splays open the $Ca_V\alpha_2\delta$-interaction site. The structures identify the $Ca_V\alpha_2\delta$-binding site for gabapentinoid anti-pain and anti-anxiety drugs[6], show that EMC and $Ca_V\alpha_2\delta$ interactions with the channel are mutually exclusive, and indicate that EMC-to-$Ca_V\alpha_2\delta$ hand-off involves a divalent ion-dependent step and $Ca_V1.2$ element ordering. Disruption of the EMC–Ca_V complex compromises Ca_V function, suggesting that the EMC functions as a channel holdase that facilitates channel assembly. Together, the structures reveal a Ca_V assembly intermediate and EMC client-binding sites that could have wide-ranging implications for the biogenesis of VGICs and other membrane proteins.

All VGIC superfamily members require assembly to make the functional channel[1,2]. High-voltage-activated Ca_Vs (Ca_V1 and Ca_V2)[3,4] are ubiquitous in electrically excitable tissues such as the muscle, brain and heart and provide a paradigmatic example of a multisubunit VGIC comprising three key components—the pore-forming $Ca_V\alpha_1$, cytoplasmic $Ca_V\beta$[5] and extracellular $Ca_V\alpha_2\delta$[6,7] subunits. It has been known for more than 30 years that $Ca_V\beta$ and $Ca_V\alpha_2\delta$ association with $Ca_V\alpha_1$ profoundly shape Ca_V biophysical properties and plasma membrane expression[5,10–13]. $Ca_V\alpha_2\delta$ has a particularly important role in enhancing cell surface expression and is the target of widely used anti-nociceptive and anti-anxiety gabapentinoid drugs[13–15] that bind to $Ca_V\alpha_2\delta$ and impair surface expression[14,16,17].

The importance of subunit assembly for the biogenesis of properly functioning channels has been long appreciated[2,18]. However, understanding of the steps involved or the extent to which chaperone proteins participate is lacking. The EMC is a nine-protein transmembrane assembly that is thought to aid the membrane insertion of tail-anchored proteins[8,9,19,20] and transmembrane segments with mixed hydrophobic/hydrophilic character, such as those in ion channels[21–23], receptors[24–26] and transporters[22,24,27]. It may also function as holdase for partially assembled membrane proteins[26]. Although recent structural studies have outlined the EMC architecture and implicated various EMC client protein interaction sites based on mutational analysis[26,28–30], there are no structural examples of EMC–client-protein complexes to guide understanding of substrate protein binding.

Here we present cryo-electron microscopy (cryo-EM) structures of an approximately 0.6 MDa complex containing the human brain and heart $Ca_V1.2$ $Ca_V\alpha_1$ subunit[3], $Ca_V\beta_3$ and human EMC, and the fully assembled $Ca_V1.2$–$Ca_V\beta_3$–$Ca_v\alpha_2\delta$-1 channel, a $Ca_V\alpha_1$–$Ca_V\beta$ combination[3,5,31] that is present in human hearts[32], at overall resolutions of 3.4 Å and 3.3 Å, respectively. This Ca_V is the target of drugs for cardiac and neurological diseases[6,7,33] and is associated with many arrhythmia, autism and neuropsychiatric disease mutations[3,4,34]. Our data provide a view of an EMC–client membrane protein complex and reveal EMC sites, the TM and Cyto docks, the interaction of which with conserved $Ca_V\alpha_1$ and $Ca_V\beta$ elements results in a partial extraction of one of the channel pore domains (PDs) relative to its native position and splaying open of the $Ca_V\alpha_1$ extracellular face where $Ca_V\alpha_2\delta$ binds. Together, the structural data indicate that EMC and $Ca_V\alpha_2\delta$ binding to the $Ca_V\alpha_1$–$Ca_V\beta$ channel

core is mutually exclusive and that EMC hand-off to $Ca_V\alpha_2\delta$ involves ordering three extracellular sites that are splayed apart in the EMC complex. Notably, disrupting EMC–channel interactions by channel mutations or EMC-subunit knockout diminishes channel activity, suggesting a role for the EMC as a Ca_V holdase. The $Ca_V1.2$–$Ca_V\beta_3$–$Ca_v\alpha_2\delta$-1 structure also reveals a bound leucine in the $Ca_V\alpha_2\delta$-binding site targeted by widely used gabapentinoid drugs[35,36] for pain, fibromyalgia, postherpetic neuralgia and generalized anxiety disorder[6,7]. Our data define a Ca_V assembly intermediate that establishes a framework for understanding Ca_V biogenesis, drug action[3,6,37] and the consequences of Ca_V disease mutations affecting the brain, heart and endocrine systems[4,34]. Owing to their conserved nature, the EMC–client interaction sites are likely to be exploited by many VGIC superfamily client proteins. Other membrane protein classes that have transmembrane segments of mixed hydrophobic and hydrophilic character[9], such as transporters and G-protein-coupled receptors, may also engage these sites.

A stable ER chaperone–ion channel complex

Purification of $Ca_V1.2(\Delta C)$—a recombinantly expressed human $Ca_V1.2$ construct bearing a C-terminal truncation distal to the Ile–Gln (IQ) domain with functional properties equivalent to full-length $Ca_V1.2$ (Supplementary Fig. 2) (186 kDa)—with rabbit $Ca_V\beta_3$ (54 kDa), yielded a sample displaying a good size-exclusion profile containing numerous unexpected bands (Extended Data Fig. 1a,b and Supplementary Fig. 1a,b). Mass spectrometry (MS) analysis showed that these bands comprise the 9 subunits of the approximately 300 kDa EMC[8,9,19] that co-purified with $Ca_V1.2(\Delta C)$–$Ca_V\beta_3$ (Supplementary Table 1a). Cryo-EM images yielded two-dimensional class averages of a transmembrane complex with an unmistakable extramembrane EMC lumenal domain crescent (Extended Data Fig. 1c,d). Co-expression of $Ca_V1.2(\Delta C)$–$Ca_V\beta_3$ with rabbit $Ca_v\alpha_2\delta$-1 (125 kDa) yielded a similarly behaved sample containing $Ca_V1.2(\Delta C)$, $Ca_V\beta_3$, $Ca_V\alpha_2\delta$-1 and all 9 EMC components (Extended Data Fig. 1e,f and Supplementary Fig. 1c,d) that also produced good cryo-EM images (Extended Data Fig. 1g,h). Single-particle analysis (Extended Data Fig. 1i) identified EMC–$Ca_V1.2(\Delta C)$–$Ca_V\beta_3$ complexes in both preparations and $Ca_V1.2(\Delta C)$–$Ca_V\beta_3$–$Ca_V\alpha_2\delta$-1 in the sample with $Ca_V1.2(\Delta C)$, $Ca_V\beta_3$ and $Ca_V\alpha_2\delta$-1. The resultant EMC–$Ca_V1.2(\Delta C)$–$Ca_V\beta_3$ and $Ca_V1.2(\Delta C)$–$Ca_V\beta_3$–$Ca_V\alpha_2\delta$-1 maps had overall resolutions of 3.4 Å and 3.3 Å (Supplementary Fig. 3a,b) and local resolutions of 2.4 Å and 2.0 Å, respectively (Extended Data Fig. 2, Extended Data Table 1 and Supplementary Figs. 3–6), and clearly defined the subunits of the eleven-protein EMC–$Ca_V1.2(\Delta C)$–$Ca_V\beta_3$ complex (Extended Data Fig. 2a,b) and the tripartite $Ca_V1.2(\Delta C)$–$Ca_V\beta_3$–$Ca_V\alpha_2\delta$-1 channel assembly (Extended Data Fig. 2c,d).

Structure of the EMC–$Ca_V1.2(\Delta C)$–$Ca_V\beta_3$ complex

The EMC–$Ca_V1.2(\Delta C)$–$Ca_V\beta_3$ complex is an approximately 0.6 MDa assembly with dimensions of about 220 Å normal to the membrane plane and around 100 Å × 130 Å parallel to the membrane plane (Fig. 1a). There are extensive $Ca_V1.2$ and $Ca_V\beta_3$ interactions with the EMC (Fig. 1a) comprising two binding sites—the TM dock and Cyto dock. These two sites are around 90° apart from each other with respect to the EMC core and

engage transmembrane and cytoplasmic elements of the $Ca_V1.2$–$Ca_V\beta_3$ channel complex, respectively (Fig. 1b,c and Supplementary Video 1).

The TM dock comprises a large interface (1,051 $Å^2$) in which the single EMC1 transmembrane helix (EMC1 TM) binds to the groove between the IS1 and IS2 transmembrane helices of the first $Ca_V1.2$ voltage-sensor domain (VSD I) (Fig. 1b–d and Extended Data Fig. 3a,b) using van der Waals interactions along the entire interface (Extended Data Fig. 3a,b) that are framed by lumenal and inner bilayer leaflet hydrophilic interaction sites (Fig. 1d). The lumenal site involves a salt bridge between Asp961 of EMC1, a conserved residue implicated in interaction with client proteins with a hydrophilic character[30], and Arg161 of $Ca_V1.2$ VSD I, a residue that is found in all Ca_V1s except for $Ca_V1.4$, and $Ca_V2.3$ (Extended Data Fig. 3c). The inner leaflet site entails a cation–π interaction[38] between the EMC1 Arg981 guanidinium and the $Ca_V1.2$ IS1 Trp123 indole that, with IS1 Ile120, frames a conserved hydrophobic pocket—the cation–π pocket (Extended Data Fig. 3a,b). Preservation of these two hydrophilic interaction sites and the IS1–IS2 surface among Ca_V1s and Ca_V2s (Extended Data Fig. 3c) suggests that other Ca_V VSDs interact similarly with the EMC. Furthermore, the interfacial EMC1 helix (brace[26] or crossbar[28] helix, hereafter brace/crossbar helix) extends its C-terminal end to contact the VSD I–PD II interface (Fig. 1c,e).

The Cyto dock (around 1,500 $Å^2$) is composed of interactions between the EMC cytoplasmic cap (EMC2, EMC3, EMC4, EMC5 and EMC8) and $Ca_V\beta_3$ (Fig. 1f) and involves two sites. In the larger site (the EMC8 site, 962 $Å^2$), two $Ca_V\beta$ nucleotide kinase domain loops (the β7–α4 loop, Thr218–Ala243; and β8–β9 loop, Pro277–Lys282) bind at a site of which the centre is formed by the last EMC8 helix (Fig. 1f). This interaction involves a hydrogen bond and salt bridge network of seven conserved $Ca_V\beta$ residues (Fig. 1f and Extended Data Fig. 3d–f) and includes a region, Lys225–Ser245, that is disordered in the isolated $Ca_V\beta_3$ (ref. 39) (Extended Data Fig. 3g) but that becomes ordered after EMC8 binding, suggesting that its conservation is linked to its EMC-binding role. In the smaller site (the EMC2 site, 550 $Å^2$), $Ca_V\beta$ contacts the EMC2 N-terminal region through van der Waals interactions (Fig. 1f and Extended Data Fig. 3f–h). This site involves $Ca_V\beta$ α5 and α6 helices that are part of the α-binding pocket where $Ca_V\beta$s make high-affinity interactions to the $Ca_V\alpha_1$ α-interaction domain (AID)[40,41]. The shared $Ca_V\beta$ architecture[40,41] and contact residue conservation indicate that all $Ca_V\beta$ isoforms should bind to the Cyto dock.

Although the TM dock site is consistent with functional data implicating EMC1 Asp961 in client protein interaction[30], the EMC1 TM–$Ca_V1.2$ VSD I interface is on the opposite side of the EMC3-, EMC5- and EMC6-gated transmembrane cavity proposed to act in membrane protein insertion[26,29,42]. The side of the channel facing the brace/crossbar helix surrounds the inner, hydrophobic, lipid-filled cavity formed by EMC1, EMC3, EMC5 and EMC6 (refs. 26,28,29,42) but, apart from the EMC1 brace/crossbar helix interactions, there are no other cavity elements interactions. The Cyto dock site is on the opposite side of the membrane from the EMC1, EMC7 and EMC10 lumenal domain elements that were previously suggested to have a holdase function[26]. Furthermore, the EMC2 and EMC8 sites are not near any cytoplasmic cap elements proposed for client interactions[28]. Thus, the structure presents an EMC–client binding mode. Importantly, $Ca_V1.2$–$Ca_V\beta_3$ interactions

with the TM dock and Cyto dock involve highly conserved channel subunit elements (Extended Data Fig. 3c,f), suggesting that Ca_Vs comprising various combinations of $Ca_V\alpha_1$ and $Ca_V\beta$[3,5] can also make the observed EMC–client interactions.

A $Ca_V\alpha_2\delta$ drug-binding site and a blocking lipid

The structure of $Ca_V1.2(\Delta C)$–$Ca_V\beta_3$–$Ca_v\alpha_2\delta$-1 (Fig. 2a, Extended Data Fig. 2c,d and Supplementary Fig. 6) reveals a tripartite channel assembly (around 370 kDa) with an overall structure similar to other Ca_V1 and Ca_V2 complexes (root mean squared deviation (r.m.s.d.)$_{C\alpha}$ = 1.95 Å, 1.71 Å and 2.37 Å for $Ca_V\alpha_1$ from $Ca_v1.1$, $Ca_v1.3$ and $Ca_v2.2$, respectively)[43–45] and $Ca_V\alpha_1$ subunit structure similar to single component Ca_V3s (r.m.s.d.$_{C\alpha}$ = 2.28 Å for $Ca_V\alpha_1$ from $Ca_v3.1$)[46] (Supplementary Fig. 7a–d). As with most Ca_V structures[43–45], the $Ca_V1.2$ pore inner gate is closed and all four voltage sensors are in the ‘up’ conformation, consistent with a depolarized state and similar to $Ca_V1.3$ (ref. 44) (Extended Data Fig. 4a–d and Supplementary Fig. 7e–h). Moreover, similar to other Ca_Vs[43–45], the proteolytic cleavage site dividing $Ca_V\alpha_2$ from $Ca_V\delta$ is disordered. Two notable features stand out. The first is a free leucine, a $Ca_V\alpha_2\delta$ ligand[6,47,48] and gabapentin competitor[6,37], in the $Ca_v\alpha_2\delta$-1 Cache1 domain[49] hydrophobic pocket of the gabapentinoid drug-binding site[6,7,35,36,50]. The high local resolution of this site (2.0–2.4 Å) shows the free leucine, obtained endogenously during expression, bound to a pocket lined by Trp207, Val209, Tyr219, Trp225, Tyr238, Arg243, Trp245, Tyr452, Asp454, Ala455, Leu456 and Asp493 (Fig. 2b, Extended Data Fig. 4e and Supplementary Fig. 6j) in agreement with the prediction of this pocket as the leucine-binding site[50]. The l-Leu backbone elements, shared with gabapentinoids[37], are coordinated through salt bridge and hydrogen bond interactions to its carboxylate by Tyr238, Arg243 and Trp245 and a salt bridge between the amino nitrogen and Asp493 (Fig. 2b and Extended Data Fig. 4e), and are consistent with the importance of Arg243 (Arg217 in some numberings)[14,51] and Asp493 (ref. 50) for gabapentinoid drug binding and action in pain modulation[14]. These data, together with studies establishing binding competition between leucine and gabapentin[6,37] and recent $Ca_V\alpha_2\delta$ structures with gabapentin[35] and mirogabalin[36] identify this Cache1 domain as the gabapentinoid drug-binding site.

The second notable feature is a lipid, phosphatidylethanolamine (PE) (1-heptadecanoyl-2-dodecanoyl-glycero-3-phosphoethanolamine (17:0/12:0)), that fills a hydrophobic gap between PD I and PD II (Fig. 2c and Supplementary Fig. 6c). The phosphatidylethanolamine hydrophilic headgroup resides in the central pore below the selectivity filter (SF), where it coordinates the inner of two SF calcium ions (Fig. 2c,d, Extended Data Fig. 4f and Supplementary Fig. 6c) that match those in $Ca_V1.1$ (refs. 43,52), $Ca_V3.1$ (ref. 46) and $Ca_V3.3$ (ref. 53). Similarly intrusive lipids between $Ca_V1.1$ PD I and PD II[52,54] and $Ca_V3.3$ PD III and PD IV[53] emerge into the central cavity in the presence of pore-blocking drugs. $Ca_V1.1$ (refs. 43,52,54) and $Ca_V3.1$ (ref. 46) structures identified lipid tails in the equivalent PD I–PD II interface but did not resolve the headgroup. Owing to its interference of the ion path in the absence of drugs, we denote the $Ca_V1.2$ phosphatidylethanolamine as the blocking lipid. The presence of the blocking lipid polar headgroup in the central cavity in direct coordination with an SF Ca^{2+} ion shows that this lipid does not require a third-party

molecule in the pore, such as a drug[52–54], and raises questions about whether and how this element contributes to channel gating and pharmacology.

Binding requires multiple rigid-body changes

Observation of the same channel complex $Ca_V1.2(\Delta C)$–$Ca_V\beta_3$ in two states—the EMC-bound form versus the fully assembled channel—reveals multiple conformational changes that substantially remodel the Ca_V structure after EMC binding (Fig. 3a and Supplementary Videos 2 and 3). The $Ca_V1.2$ VSD I, VSD II and VSD IV S4 segments correspond to a voltage sensor 'up' state in which gating charge residues (VSD I: K1, R2, R3 and R4; VSD II: R2, R3 and R4; and VSD IV: R2, R3 and R4) are on the extracellular/lumenal side of the aromatic position that defines the charge transfer centre[55] (Supplementary Fig. 8a–c). Although VSD I and VSD II are similar to those in $Ca_V1.2(\Delta C)$–$Ca_V\beta_3$–$Ca_v\alpha_2\delta$-1 (Supplementary Fig. 8d,e) ($r.m.s.d._{C\alpha}$ = 0.69 Å and 2.25 Å for VSD I and VSD II, respectively) both undergo substantial rigid body displacements after EMC binding (Fig. 3a and Supplementary Videos 2–5). VSD III and VSD IV (Supplementary Fig. 8f) ($r.m.s.d._{C\alpha}$ = 2.35 Å for VSD IV) undergo various degrees of rearrangement (Fig. 3a and Supplementary Videos 2, 3 and 6), the most notable of which is the unfolding of the majority of VSD III (Fig. 3a).

Viewed from the IS1–IS2 groove, VSD I rotates about 20° around an axis parallel with the membrane plane towards the channel periphery to engage the EMC1 TM helix (Supplementary Videos 2 and 4) and rotates approximately 10° within the membrane plane towards VSD IV (Fig. 3a and Extended Data Fig. 5a). VSD II tips away from the central pore by about 15° resulting in a displacement of the extracellular/lumenal ends of its helices by around 6 Å (Fig. 3a, Extended Data Fig. 5a and Supplementary Video 5). With the exception of the S4 C-terminal end, VSD III is largely disordered in the EMC–Ca_V complex. This lack of structure is apparent in the detergent micelle shape surrounding the channel (Extended Data Fig. 2b and d). VSD IV undergoes a complex set of changes in which S3 and S4 are repositioned relative to the S1–S2 pair, and rotates about 10° within the plane of the membrane towards VSD I (Fig. 3a, Extended Data Fig. 5a and Supplementary Videos 2 and 6). Thus, the relative conformations of all four VSDs change as a consequence of EMC binding.

Three out of the four PDs in the EMC complex are also altered relative to $Ca_V1.2(\Delta C)$–$Ca_V\beta_3$–$Ca_v\alpha_2\delta$-1. The most marked change is PD III. This PD is partially extracted from the central pore and displaced towards the channel periphery by around 5 Å (Fig. 3a, Extended Data Fig. 5b and Supplementary Videos 2 and 3). Notably, despite some internal shifts ($r.m.s.d._{C\alpha}$ = 3.269 Å), the PD III tertiary fold comprising the IIIS5, PH1 and IIIS6 helices retains a near-native conformation (Extended Data Fig. 5b and Supplementary Video 7), consistent with the recent demonstration that the VGIC PD tertiary structure is independent of the quaternary structure[56]. PD III PH2 is displaced by around 15° and the large extracellular loops connected to it are disordered. The other PD tertiary structures are largely unaltered ($r.m.s.d._{C\alpha}$ = 0.91 Å, 0.46 Å and 1.17 Å for PD I, PD II and PD IV, respectively) but, as a consequence of PD III extraction, PD II and PD IV undergo rigid-body changes, tipping towards and away from the pore central axis, respectively

(Supplementary Videos 2, 3, 8 and 9). Extraction of PD III pulls the domain III S4–S5 linker along the lateral side of the channel by one helical turn, approximately 6 Å (Fig. 3b and Supplementary Video 3), disturbing VSD III and leading to its unfolding (Fig. 3a and Extended Data Fig. 5a).

Binding to EMC reshapes the channel pore

Comparison of $Ca_V\beta_3$ in the EMC and $Ca_V1.2(\Delta C)$–$Ca_V\beta_3$–$Ca_v\alpha_2\delta$-1 complexes reveals conformational changes associated with EMC intracellular cap binding that explain the mechanism of PD III extraction from the central pore. To bind to the Cyto dock, $Ca_V\beta_3$ rotates about 5° away from its $Ca_V1.2(\Delta C)$–$Ca_V\beta_3$–$Ca_v\alpha_2\delta$-1 position close to the membrane (Fig. 3a and Extended Data Fig. 5c) and transmits this conformational change to the channel through the $Ca_V1.2$ AID helix. This element remains bound to $Ca_V\beta_3$ and tilts about 15° away from the membrane plane, displacing its C-terminal end by approximately 11 Å relative to its $Ca_V1.2(\Delta C)$–$Ca_V\beta_3$–$Ca_v\alpha_2\delta$-1 position (Fig. 3a and Extended Data Fig. 5c) and enabling four AID acidic residues (Asp439, Glu445, Asp446 and Asp448) opposite to its $Ca_V\beta_3$ interface to interact with five VSD II IIS0 helix basic residues (Arg507, Arg511, Arg514, Arg515 and Arg518) (Fig. 3c). This interaction is absent in $Ca_V1.2(\Delta C)$–$Ca_V\beta_3$–$Ca_v\alpha_2\delta$-1 (Extended Data Fig. 5d) and occurs because IIS0 becomes more helical in the EMC complex (Extended Data Fig. 5d). These electrostatic interactions provide a link that pulls VSD II away from the channel central axis as a consequence of AID tilt (Fig. 3a). As VSD II IIS1 and IIS4 extracellular/lumenal ends make numerous contacts with PD III IIIS5 and PH1 (Fig. 3c and Extended Data Fig. 5e) that are maintained in both structures, VSD II movement pulls PD III away from the central pore. The PD III–VSD II–AID–$Ca_V\beta_3$ assembly therefore acts as single unit of which the positions are transformed by the EMC–$Ca_V\beta_3$ interaction to effect the partial extraction of PD III from the central pore assembly, displacement of helical S4–S5 linker between IIIS4 and IIIS5 by about 6 Å (Supplementary Videos 2 and 3) and VSD III destabilization (Fig. 3a,b).

PD III extraction substantially reshapes the ion-conduction pathway. The overall pore diameter increases due to changes at its two narrowest points—the SF and inner gate (Fig. 4a,b and Extended Data Fig. 6)—that widen by about 1.1 Å and 1.0 Å, respectively, to create a water-filled pore that bridges the channel cytoplasmic and lumenal sides (Fig. 4b and Extended Data Fig. 6). SF expansion affects the SF glutamate ring outer ion coordination site (Glu363, Glu706, Glu1115 and Glu1416) (Fig. 4c), while inner gate widening creates a pathway in which we find density for a bound glycol-diosgenin (GDN) (Fig. 4d–g, Extended Data Fig. 6 and Supplementary Fig. 4f). This GDN sits at a position similar to that seen in a drug-bound $Ca_V1.1$–verapamil complex with a widened inner gate[52] and may mimic a natural lipid similar to GDN, such as cholesterol, that would serve as a plug to prevent ion leak through the EMC-bound pore. We therefore denote this as the lipid plug (Fig. 4d,f,g). Thus, association between the $Ca_V1.2$–$Ca_V\beta_3$ complex and the EMC pulls and twists various channel elements, mostly through rigid-body domain movements, that splay open the central pore.

Brace/crossbar helix is raised to an up position

A comparison with structures of the human EMC determined in lipid nanodiscs[26,29] shows that $Ca_V1.2$–$Ca_V\beta_3$ binding causes a conformational change in the EMC lumenal domain, comprising EMC1, EMC4, EMC7 and EMC10, in which the EMC top β-propeller domain moves by around 11.5 Å lateral to the membrane plane (Supplementary Fig. 9a–d). This tilt lifts and translates the EMC1 brace/crossbar helix towards the client by approximately 6 Å and 10 Å, respectively (Supplementary Fig. 9a–d and Supplementary Videos 10 and 11), enabling it to engage the VSD I–PD II interface (Fig. 1e) in an interaction that induces the folding of one helical turn at the brace/crossbar helix C-terminal end (residues Trp503–Tyr507) (Fig. 1e and Supplementary Fig. 9c,d). We designate this as the up conformation. The remainder of the EMC complex is largely unchanged, with the exception of clockwise rotations of the EMC3, EMC5 and EMC6 transmembrane elements (r.m.s.d.$_{C\alpha}$ = 1.44 Å, 0.91 Å and 0.63 Å for EMC3, EMC5 and EMC6, respectively) and a slight counterclockwise repositioning of the EMC1 TM (r.m.s.d.$_{C\alpha}$ = 0.62 Å) (Supplementary Fig. 9b and Supplementary Video 12). By contrast, in the detergent complex lacking EMC7 (ref. 26), the lumenal domain and brace/crossbar helix are in an up position similar to in the EMC–$Ca_V1.2(\Delta C)$–$Ca_V\beta_3$ complex (Supplementary Fig. 9e) (r.m.s.d.$_{C\alpha}$ = 0.84 Å), even though its C-terminal helical structure is shorter than that in the EMC–$Ca_V1.2(\Delta C)$–$Ca_V\beta_3$ complex and stops at Leu502. These conformational differences suggest that brace/crossbar helix client engagement stabilizes the up position by biasing the apo-EMC conformational landscape. EMC1 up-state stabilization could enable endoplasmic reticulum lumen chaperones to recognize client-loaded EMCs and signal its holdase function, consistent with proposals that the different EMC conformations are associated with client-loaded states[26].

EMC and $Ca_V\alpha_2\delta$ binding is mutually exclusive

Superposition of the EMC–$Ca_V1.2(\Delta C)$–$Ca_V\beta_3$ complex and $Ca_V1.2$–$Ca_V\beta_3$–$Ca_V\alpha_2\delta$-1 shows that the EMC and $Ca_V\alpha_2\delta$ interact with $Ca_V1.2$ in a mutually exclusive manner (Extended Data Fig. 7a). There are clashes with $Ca_V\alpha_2\delta$-1 all along the lumenal parts of EMC1 as well as with the EMC1 brace/crossbar helix (Extended Data Fig. 7a,b). Notably, three EMC-bound $Ca_V1.2$ elements that are displaced from their positions in $Ca_V1.2(\Delta C)$–$Ca_V\beta_3$–$Ca_V\alpha_2\delta$-1, VSD I, PD II and PD III, each interact with $Ca_V\alpha_2\delta$ in the fully assembled channel (Extended Data Fig. 7c). Rigid-body rotation of VSD I between its EMC-bound and $Ca_V\alpha_2\delta$-bound positions (Fig. 3a) moves Asp151 about 5 Å to complete the coordination sphere of the calcium ion bound to the $Ca_V\alpha_2\delta$ von Willebrand factor type A (VWA) domain metal-ion-dependent adhesion site (MIDAS) (Extended Data Fig. 7c). This VSD I residue is conserved in Ca_V1s and Ca_V2s (Extended Data Fig. 3c) and its equivalent coordinates a similar $Ca_V\alpha_2\delta$-bound Ca^{2+} in $Ca_V1.1$ (ref. 43) and $Ca_V2.2$ (ref. 45). $Ca_V\alpha_2\delta$ VWA MIDAS coordination of divalent ions is critical for $Ca_V\alpha_2\delta$ binding to $Ca_V1.2$ (ref. 57) and $Ca_V2.2$ (ref. 58) and for the ability of $Ca_V\alpha_2\delta$ to promote $Ca_V1.2$, $Ca_V2.1$ and $Ca_V2.2$ plasma membrane trafficking[57–59]. We therefore denote this tripartite interaction as the divalent staple owing to its importance for assembled state stabilization.

Movement of PD II and PD III to their $Ca_V1.2$–$Ca_V\beta_3$–$Ca_v\alpha_2\delta$-1 positions and restoration of PD intersubunit interactions (Fig. 3b and Extended Data Fig. 7d) appears to be linked to establishment of interactions with the $Ca_V\alpha_2\delta$ VWA and Cache1 domains, respectively (Extended Data Fig. 7c), and agrees with the importance of PD III for $Ca_V\alpha_2\delta$ binding[60]. Notably, the large PD III extracellular loops linking PH1–IS5 and PH2–IS6 are disordered in the EMC–$Ca_V1.2(\Delta C)$–$Ca_V\beta_3$ complex but make extensive interactions with $Ca_V\alpha_2\delta$ binding (Extended Data Fig. 7c), indicating that the folding of these elements is $Ca_V\alpha_2\delta$ dependent. This interaction, together with divalent staple coordination, is central to the consolidation of the native $Ca_V1.2$–$Ca_V\beta_3$–$Ca_v\alpha_2\delta$-1 assembly and suggests that the hand-off of the $Ca_V1.2$–$Ca_V\beta_3$ complex from the EMC holdase to $Ca_V\alpha_2\delta$ is a critical step in channel assembly.

$Ca_V\beta$ stablizes $Ca_V\alpha_1$ binding to the EMC

The strong association of the $Ca_V1.2(\Delta C)$–$Ca_V\beta_3$ complex and EMC (Extended Data Figs. 1a and 8a) prompted us to examine whether individual channel subunits could bind to the EMC. We expressed $Ca_V1.2(\Delta C)$ or $Ca_V\beta_3$ and then performed a purification procedure similar to the one that yielded the EMC–$Ca_V1.2(\Delta C)$–$Ca_V\beta_3$ complex to assay EMC complex formation. Purified $Ca_V1.2(\Delta C)$ yielded a broader SEC peak than the EMC–$Ca_V1.2(\Delta C)$–$Ca_V\beta_3$ complex (Extended Data Fig. 8a,b) and contained EMC subunits identified by SDS–PAGE and MS (Extended Data Fig. 8b,c, Supplementary Fig. 1e,f and Supplementary Table 1a). A quantitative comparison found lower proportions of EMC subunits relative to $Ca_V1.2(\Delta C)$ than those observed for the EMC–$Ca_V1.2(\Delta C)$–$Ca_V\beta_3$ complex (Extended Data Fig. 8c), suggesting that $Ca_V1.2(\Delta C)$ binds to the EMC less tightly. By contrast, $Ca_V\beta_3$ purification yielded no EMC subunits (Extended Data Fig. 8d,e, Supplementary Fig. 1g and Supplementary Table 1a). This sample had two lower-molecular-mass bands corresponding to the $Ca_V\beta_3$ nucleotide kinase and SH3 domains (Extended Data Fig. 8d and Supplementary Fig. 1g), which are known to associate[40,61] and probably result from proteolytic cleavage. Thus, these data indicate that the Ca_V pore-forming subunit can stably associate with the EMC and that this association is strengthened by $Ca_V\beta$ binding, consistent with the multipoint nature of EMC–$Ca_V1.2(\Delta C)$–$Ca_V\beta_3$ interactions. Such interactions may explain the ability of $Ca_V\beta$ subunits to protect $Ca_V1.2$ (ref. 62) and $Ca_V2.2$ (ref. 63) pore-forming subunits from proteasome and ERAD pathway[62] degradation in a variety of cell types, including neurons[62,63].

The $Ca_V1.2$ distal C-terminal tail affects forward trafficking[64]. To test whether this region, absent from the EMC–$Ca_V1.2(\Delta C)$–$Ca_V\beta_3$ structure, might influence EMC binding, we expressed and purified the full-length $Ca_V1.2$–$Ca_V\beta_3$ complex. Similar to the $Ca_V1.2(\Delta C)$ used in structure determination, this full-length subunit combination binds strongly to the EMC (Extended Data Fig. 8f,g, Supplementary Table 1b and Supplementary Fig. 1h), underscoring the biochemical stability of the EMC–$Ca_V1.2$–$Ca_V\beta_3$ complex and further supporting the idea that this complex may be important for channel biogenesis.

EMC–Ca_V disruption compromises channel function

To test the idea that the EMC functions as a channel holdase, we designed $Ca_V1.2$ and $Ca_V\beta_3$ mutants that perturbed the $Ca_V1.2$–TM dock and $Ca_V\beta$–Cyto dock sites (Fig. 5a,b). These included a tri-Ala mutation of $Ca_V1.2$ residues making charge and cation–π interactions with the EMC1 TM dock site (R161A, I120A and W123A; $Ca_V1.2$(ΔC:3A)) (Fig. 5a), a penta-Ala $Ca_V\beta_3$ mutant at the Cyto dock EMC2 site (M312A, L315A, T316A, M319A and D323A; $Ca_V\beta_3$(5A)), a deletion of the $Ca_V\beta_3$ loop that interacts with the EMC8 site ($Ca_V\beta_3$(Δ220–240)) (Fig. 5b) and two mutants affecting both the EMC2 and EMC8 Cyto dock sites, an undeca-Ala $Ca_V\beta_3$ mutant of all Cyto dock contacts (D220A, R226A, K234A, R240A, Q301A, R305A, M312A, L315A, T316A, M319A and D323A; $Ca_V\beta_3$(11A)) (Fig. 5b) and a combination of the 5A and Δ220–240 mutants ($Ca_V\beta_3$(5A:Δ220–240)) (Fig. 5b). We next examined the functional consequences using whole-cell recording of HEK293 cells transfected with various $Ca_V1.2$ and $Ca_V\beta_3$ subunit combinations expressed with $Ca_V\alpha_2\delta$-1.

Disruption of interactions in the TM dock by $Ca_V1.2$(ΔC:3A) or the large EMC8 site by $Ca_V\beta_3$(Δ220–240) reduced current levels by around 50% (Fig. 5c,d), whereas disruption of the smaller EMC2 site, $Ca_V\beta_3$(5A), was not different from the control $Ca_V1.2$(ΔC)–$Ca_V\beta_3$ pair. Notably, complete Cyto dock site disruption by $Ca_V\beta_3$(5A:Δ220–240) or $Ca_V\beta_3$(11A) reduced Ca_V currents by around 90% relative to the control, mirroring the effects of the absence $Ca_V\beta_3$, of which the presence is essential for Ca_V plasma membrane expression[5,10,11,62,65–67]. In all cases, the measurable channels had biophysical properties matching the parent $Ca_V1.2$(ΔC)–$Ca_V\beta_3$ pair, with the exception of channels bearing $Ca_V\beta_3$(Δ220–240) and $Ca_V\beta_3$(5A:Δ220–240), which showed a small (around 7 mV) positive shift in activation voltage dependence (Extended Data Fig. 9a and Supplementary Table 2). Thus, these data indicate that EMC binding-site mutations affect channel function primarily by reducing plasma membrane expression and support the idea that the complex represents a productive step in functional Ca_V assembly.

We next purified $Ca_V1.2$(ΔC)–$Ca_V\beta_3$(11A), a mutant that substantially reduced channel expression but spared channel biophysical properties (Extended Data Fig. 9a and Supplementary Table 2), and quantified its association with the EMC using MS (Extended Data Fig. 9b,c, Supplementary Fig. 1i,j and Supplementary Table 1c). These data show that ablation of the Cyto dock interactions greatly reduces (around 90%) EMC binding relative to $Ca_V1.2$(ΔC)–$Ca_V\beta_3$ and matches the EMC-binding loss observed for $Ca_V1.2$(ΔC) in the absence of $Ca_V\beta_3$ (Extended Data Fig. 8b,c). Taken together, the common effects that $Ca_V\beta$ Cyto dock site disruption or $Ca_V\beta$ absence have on EMC association and channel function (Fig. 5c and Extended Data Figs. 8a–e and 9b,c) indicate a key role of $Ca_V\beta$–Cyto dock interactions in EMC–Ca_V complex formation and channel functional expression.

We next examined Ca_V function in HEK293 knockout cell lines lacking EMC subunits of which the absence disrupts the EMC[20]. We tested cells lacking EMC5 (*EMC5* knockout)[20,68], a transmembrane subunit that supports the EMC1 brace/crossbar helix that interacts with $Ca_V1.2$ and that scaffolds the Cyto dock EMC2 and EMC8 subunits; or EMC6 (*EMC6* knockout)[20,68], a transmembrane subunit further from the EMC–Ca_V

interface (Fig. 5e). Whole-cell recording (Fig. 5c,f) shows that *EMC5* knockout (Fig. 5e) eliminates channel functional expression, whereas *EMC6* knockout partially suppresses channel functional expression. Importantly, channels expressed in *EMC6*-knockout cells were biophysically indistinguishable from channels expressed in unmodified HEK293 cells (Extended Data Fig. 9a and Supplementary Table 2), indicating that the loss of plasma membrane functional expression is a consequence of a loss of EMC–channel interactions and not a general effect. The ability of the EMC knockouts to phenocopy the effects of EMC–channel interface mutations together with the consequences of channel mutations in the EMC–Ca_V binding sites provides further evidence that the EMC and its interactions with the channel are essential for functional Ca_V expression.

Discussion

The profound effects that the intracellular $Ca_V\beta$[5] and extracellular $Ca_V\alpha_2\delta$[6,7] auxiliary subunits have on Ca_V1 and Ca_V2 function and trafficking are well known[5,10–13,15]. Yet, apart from the role of the $Ca_V\beta$–AID interaction in folding the $Ca_V\alpha_1$ AID helix[41,69], there is scant structural information regarding how $Ca_V\beta$ and $Ca_V\alpha_2\delta$ act during channel biogenesis and assembly. The identification of the EMC–$Ca_V1.2(\Delta C)$–$Ca_V\beta_3$ complex, the evidence that $Ca_V1.2$ can bind to the EMC alone and the demonstration that EMC–Ca_V interactions affect functional channel expression offer direct insights into this process and suggest a mechanism by which the EMC acts as a holdase for the channel—a function that is probably relevant for diverse classes of membrane protein clients.

Various EMC domains have been suggested to function in transmembrane segment insertion into the lipid bilayer[26,28,29,42] or serve as holdase sites[26]. Notably, none of these elements form the TM dock and Cyto dock sites that bind to $Ca_V1.2(\Delta C)$–$Ca_V\beta_3$, a membrane protein complex with a different topology compared with EMC tail-anchored protein clients[9]. Thus, our EMC–client structure expands the idea that the EMC uses diverse elements for different functions[26]. The EMC1 TM dock uses a lumenal-side salt bridge to an EMC1 residue implicated in client binding, Asp961 (ref. 30), and a cytoplasmic-side cation–π interaction[38] with EMC1 Arg981 (Extended Data Fig. 3a,b) to bind to the $Ca_V1.2$ VSD I (Fig. 1b–d and Extended Data Fig. 3a–c). The conserved nature of this interface strongly suggests that other Ca_V1s and Ca_V2s interact with the EMC. The observation that the $Ca_V\alpha_1$ subunit appears to bind to the EMC complex on its own (Extended Data Fig. 8b) suggests that EMC interactions with VSD I, the first channel transmembrane domain to be synthesized during translation[2,18], may be an early stabilization step during biogenesis. Augmentation of the TM dock site by VSD I and PD II interactions with the EMC1 brace/crossbar helix interactions that induce the up conformation of the EMC lumenal subassembly (EMC1/4/7/10) (Supplementary Fig. 9a,c,d) may signal the client-loaded status of the EMC to lumenal factors or other chaperones[26]. Taken together, these findings define the TM dock as a hub of EMC holdase function.

$Ca_V\beta$ binding to the EMC Cyto dock involves EMC2 and EMC8 regions that were not to our knowledge previously known to bind to clients, and establishes the EMC intracellular domain as an important EMC–client interaction site. $Ca_V\beta$ interaction with the Cyto dock is critical for EMC binding (Extended Data Fig. 9b,c) and Ca_V functional expression

(Fig. 5c,d), suggesting that EMC–Ca_V complex stabilization by $Ca_V\beta_3$ is a key step for functional channel formation. $Ca_V\beta$ binding to pore-forming $Ca_V\alpha_1$ subunits not only increases cell surface expression of Ca_V1 (refs. 62,65,66) and Ca_V2 (ref. 67) channels but also protects $Ca_V\alpha_1$ subunits from degradation by the proteasome[63] and the ERAD pathway[62]. Taken together, these observations suggest the EMC–channel complex protects the partly assembled channel from degradation and points to a new mechanism by which $Ca_V\beta$ binding influences the fate of $Ca_V\alpha_1$ subunits.

The most substantial structural consequence of the EMC–$Ca_V\beta$ interaction is the orchestration of the coordinated displacement of $Ca_V1.2$ pore-forming subunit AID, VSD II and PD III elements in a manner that causes partial extraction of PD III from the channel pore (Fig. 3a, Extended Data Fig. 5b and Supplementary Videos 2 and 3). Together with the rotation of VSD I away from its native position, these changes substantially reshape the extracellular portions of the channel adjacent to the EMC relative to their conformations in the $Ca_V1.2(\Delta C)$–$Ca_V\beta_3$–$Ca_V\alpha_2\delta$-1 complex. As the EMC and $Ca_V\alpha_2\delta$-1 bind to the same side of the $Ca_V\alpha$–$Ca_V\beta$ core in a mutually exclusive manner (Extended Data Fig. 7a), these conformational changes suggest that the role of the EMC is to prepare the $Ca_V\alpha$–$Ca_V\beta$ complex for $Ca_V\alpha_2\delta$ binding.

Association of $Ca_V\alpha_2\delta$ with the pore-forming subunit channel is governed by $Ca_V\alpha_2\delta$ VWA MIDAS Ca^{2+} binding during a step that is thought to occur in the endoplasmic reticulum lumen[59] and is crucial for trafficking[17,70]. In agreement with these observations, our structural data point to a central role for the divalent staple that bridges the $Ca_V\alpha_2\delta$ VWA MIDAS domain and VSD I in the transition between the EMC-bound and $Ca_V\alpha_2\delta$-bound complexes. The structures show that $Ca_V\alpha$–$Ca_V\beta$ complex hand-off from the EMC to $Ca_V\alpha_2\delta$ involves a rigid body rotation of VSD I that enables the conserved Asp151, which is crucial for $Ca_V\alpha_2\delta$-dependent Ca_V1 (ref. 57) and Ca_V2 (ref. 58) trafficking, to complete the divalent staple coordination sphere (Extended Data Figs. 3c and 7c) and stabilize interaction with $Ca_V\alpha_2\delta$. In agreement with the importance of PD III in $Ca_V\alpha_2\delta$ binding[60], such an exchange would permit the extracellular PD III loops that are disordered in the EMC–$Ca_V1.2$–$Ca_V\beta_3$ complex to form extensive interactions with $Ca_V\alpha_2\delta$ VWA and Cache1 domains (Extended Data Fig. 7c). Establishing native $Ca_V\alpha_2\delta$ interactions with PD III would require $Ca_V\beta$ release from the Cyto-dock and expulsion of the lipid plug (Fig. 4d,f,g) as the pore closes. Whether such steps happen in an ordered manner or in an EMC–$Ca_V\alpha_2\delta$ capture–release competition are important unanswered questions. Taken together, our data strongly suggest that the extensive conserved interactions of $Ca_V\alpha$ and $Ca_V\beta$ subunits with the EMC have a role in the ability of $Ca_V\alpha_2\delta$ to promote trafficking of Ca_V1s and Ca_V2s[10,13,71], indicate that this exchange is a key step in channel biogenesis and quality control, and provide a framework to study Ca_V biogenesis. Exchange between the EMC holdase and $Ca_V\alpha_2\delta$ is likely also to be influenced by Ca_V domains that enhance forward trafficking[64], Ca_V-directed drugs[6,7,33], especially the gabapentinoids that target $Ca_V\alpha_2\delta$[14,16,17], and Ca_V subunit disease mutations[4,5,34]. These factors require further investigation.

The EMC is linked to the biogenesis of a variety of ion channels[21–23], including one VGIC superfamily member[22]. Given the conserved structure of VSD within the VGIC

superfamily[1], the EMC may participate in the biogenesis of other VGICs through TM dock interactions similar to those defined here. By contrast, binding of the Cyto dock site involves a unique Ca_V1 and Ca_V2 subunit, $Ca_V\beta$[5]. Interaction with this part of the EMC largely involves a $Ca_V\beta$ loop structure that is important for EMC-dependent functional expression (Fig. 5) and could have structural equivalents in other proteins. Defining the roles of the TM and Cyto dock sites for binding to Ca_Vs and other clients is an important line of study enabled by the framework presented here. It will also be essential to test whether other classes of clients engage these newly defined sites or interact with other, yet to be defined, EMC client-binding sites. Furthermore, many VGICs bear disease mutations that are not easily rationalized based on mature channel structure. Some of these mutations may disturb EMC interactions that are crucial for channel assembly, maturation and quality control. The structural framework described here sets the stage for detailed mechanistic studies into the structural basis of trafficking and assembly of VGICs and other membrane proteins that are thought to interact with the EMC[9].

Online content

Any methods, additional references, Nature Portfolio reporting summaries, source data, extended data, supplementary information, acknowledgements, peer review information; details of author contributions and competing interests; and statements of data and code availability are available at https://doi.org/10.1038/s41586-023-06175-5.

Methods

Expression and purification of human $Ca_v1.2$ and $Ca_v1.2$-loaded human EMC complex

Codon-optimized cDNAs of human $Ca_V1.2$(full length) (2,138 residues; UniProt: Q13936–20); human $Ca_v1.2$ bearing a C-terminal truncation at residue 1648 ($Ca_V1.2(\Delta C)$), a site 13 residues after the end of the IQ domain (Δ1649–2138; UniProt: Q13936–20, 1,648 residues) followed by a 3C protease cleavage site, monomeric enhanced green fluorescent protein (mEGFP) and a His_8 tag; rabbit $Ca_v\alpha_2\delta$-1 (1,105 residues; UniProt: P13806–1); and rabbit $Ca_V\beta_3$ (477 residues; UniProt: P54286) followed by a Strep-tag II sequence[74] were synthesized (GenScript) and each was subcloned into a modified pFastBac expression vector in which the polyhedrin promoter was replaced with a mammalian cell active CMV promoter[75]. The expression vector for $Ca_V\beta_3$(11A) was generated by site-directed mutagenesis in pFastBac. All of the constructs were sequenced completely. The Strep-tag-bearing rabbit $Ca_V\beta_3$ construct was used to generate a stable cell line in HEK293S GnTI$^-$ (ATCC) using a lentiviral system as described previously[76] and denoted as $Ca_V\beta_3$-stable.

Chemically competent DH10EmBacY (Geneva Biotech) cells were used to generate the recombinant bacmid DNA, which was then used to transfect *Spodoptera frugiperda* (Sf9) cells to make baculoviruses for each subunit[77]. For structural and biochemical studies, $Ca_V1.2$ (full length) and $Ca_V1.2(\Delta C)$ were expressed in $Ca_V\beta_3$-stable cells alone or together with $Ca_v\alpha_2\delta$-1 using a baculovirus transduction-based system[77]. For pull-down studies, $Ca_v1.2$, $Ca_V\beta_3$ or both were expressed in unmodified HEK293S GnTI$^-$ cells. $Ca_V\beta_3$-stable and HEK293S GnTI$^-$ cells were grown in suspension at 37 °C supplied with 8% CO_2 in FreeStyle 293 Expression Medium (Gibco) supplemented with 2% fetal bovine serum (Peak

Serum), and were transduced with 5% (v/v) baculovirus for each target subunit when the cell density reached around 2.5×10^6 cells per ml. Sodium butyrate (10 mM) was added to cell culture 16–24 h after transduction and the cells were subsequently grown at 30 °C. Cells were collected 48 h after transduction by centrifugation at 5,000*g* for 30 min. The pellet was washed with Dulbecco's phosphate-buffered saline (Gibco) and stored at −80 °C.

A cell pellet (from around 3.6 l culture) was resuspended in 200 ml of resuspension buffer containing 0.3 M sucrose, 1 mM ethylenediaminetetraacetic acid, 10 mM Tris-HCl, pH 8.0 supplemented with 1 mM phenylmethylsulfonyl fluoride and 4 Pierce protease inhibitor tablets (Thermo Fisher Scientific), then stirred gently on the Variomag magnetic stirrer MONO DIRECT (Thermo Fisher Scientific) at 4 °C for 30 min. The membrane fraction was collected by centrifugation at 185,500*g* for 1 h and subsequently solubilized in 200 ml of solubilization buffer (buffer S) containing 500 mM NaCl, 5% glycerol (v/v), 0.5 mM $CaCl_2$, 20 mM Tris-HCl, pH 8.0, supplemented with 1% (w/v) GDN, and rotated on the Orbitron rotator II (speed mode S) (Boekel Scientific) at 4 °C for 2 h. The supernatant, collected by centrifugation at 185,500*g* for 1 h, was diluted with an equal volume of buffer S to a final concentration of 0.5% GDN and incubated with anti-GFP nanobody Sepharose resin[78] at 4 °C overnight. The resin was loaded onto an Econo-Column chromatography column (BioRad) and then was then washed stepwise with 20 column volumes (CV) of buffer S supplemented with 0.1% (w/v) GDN, 20 CV of buffer S supplemented with 0.02% (w/v) GDN, and 20 CV of elution buffer (buffer E) containing 150 mM NaCl, and 0.5 mM $CaCl_2$, 0.02% (w/v) GDN 20 mM, Tris-HCl pH 8.0. The protein was eluted with 3C protease[79] and subsequently incubated at 4 °C for 2 h with 4 ml of Strep-tactin Superflow Plus beads (Qiagen) pre-equilibrated with buffer E. The beads were washed with 20 CV of buffer E and the protein was eluted with buffer E supplemented with 2.5 mM desthiobiotin. The eluent was concentrated using an Amicon Ultra-15 100-kDa cut-off centrifugal filter unit (Merck Millipore) before purification using the Superose 6 Increase 10/300 GL gel filtration column (GE Healthcare) pre-equilibrated in buffer E. Peak fractions were pooled for MS analysis and concentrated using the Amicon Ultra 0.5 ml 100 kDa cut-off centrifugal filter unit (Merck Millipore) for cryo-EM sample preparation (1.7 mg ml^{-1} $Ca_v1.2(\Delta C)$–$Ca_v\beta_3$ sample or 2.7 mg ml^{-1} $Ca_v1.2(\Delta C)$–$Ca_v\beta_3$–$Ca_v\alpha_2\delta$-1 sample).

Two-electrode voltage-clamp electrophysiology

The C-terminally truncated human $Ca_v1.2$ (Δ1649–2138; $Ca_v1.2(\Delta C)$) construct was obtained from a full-length human $Ca_v1.2$ (UniProt: Q13936–20) template in pcDNA3.1 (Invitrogen) using the Gibson Assembly kit (NEB). Full-length $Ca_v1.2$ or $Ca_v1.2(\Delta C)$ was co-expressed with rabbit $Ca_V\beta_3$ (UniProt: P54286) in pcDNA3.1 for *Xenopus* oocyte two-electrode voltage-clamp experiments. A total of 5 μg of $Ca_v1.2$ or $Ca_v1.2(\Delta C)$ and $Ca_V\beta_3$ cDNA was linearized using 30 U of the restriction enzymes XhoI and NotI (NEB), respectively, at 37 °C overnight. The linearized cDNA was used as the template to synthesize capped mRNA using the T7 mMessenger kit (Ambion). A total of 100 nl of $Ca_v1.2$ or $Ca_v1.2(\Delta C)$ and $Ca_V\beta_3$ mixed at a 1:1 molar ratio was injected into *Xenopus* oocytes 1–2 days before recording. Two-electrode voltage-clamp experiments were performed as previously described[80]. In brief, oocytes were injected with 50 nl of 100 mM BAPTA 2–4 min before recording to minimize calcium-activated chloride currents[80,81].

For recording of Ca^{2+} or Ba^{2+} currents, bath solutions contained 50 mM NaOH, 40 mM $Ca(NO_3)_2$ or 40 mM $Ba(OH)_2$, respectively, 1 mM KOH, 10 mM HEPES, adjusted to pH 7.4 with HNO_3. Electrodes were filled with 3 M KCl and had resistances of 0.3–1.0 MΩ. Recordings were conducted at room temperature from a holding potential of −90 mV. Leak currents were subtracted using a P/4 protocol.

Oocytes were collected from female *Xenopus laevis* (Nasco, LM00531) and housed in the UCSF Laboratory Animal Resource Center (LARC) facilities. The use of these *Xenopus* oocytes was approved by IACUC (protocol approval, AN193390–01B) and experiments were performed in accordance with University of California guidelines and regulations.

Whole-cell patch-clamp electrophysiology

Whole-cell patch-clamp experiments were performed as previously described[80] using pcDNA3.1 vectors for $Ca_V1.2$ (UniProt: Q13936–20) and rabbit $Ca_V\alpha_2\delta$-1 (UniProt: P13806–1)[80], and pTracer-CMV2-GFP (Thermo Fisher Scientific, V88520) for rabbit $Ca_V\beta_3$ (UniProt: P54286). $Ca_V1.2$ and $Ca_V\beta_3$ mutants were generated by site-directed mutagenesis. Human embryonic kidney cells (HEK293, ATCC, CRL-1573) and HEK293FT cell lines[20,68] (WT, *EMC5* knockout and *EMC6* knockout) were grown at 37 °C under 5% CO_2 in a Dulbecco's modified Eagle's medium supplemented with 10% fetal bovine serum, 1% l-glutamine, 1% (v/v) GlutaMAX, 1% (v/v) sodium pyruvate, 1% (v/v) MEM non-essential amino acids and antibiotics (100 IU ml^{-1} penicillin and 100 mg ml^{-1} streptomycin). HEK293 cells and HEK293FT cells were transfected (in 35 mm diameter wells of Corning 6-well flat-bottom culture plates) with Lipofectamine 2000 (Invitrogen) and plated onto coverslips coated with Matrigel (BD Biosciences).

Cells were transfected using a total of 4.6 μg DNA with a ratio by weight of 2:0.9:1.3:0.4 of $Ca_V\alpha_1$:$Ca_V\beta_3$:$Ca_V\alpha_2\delta$-1:sv40 T-antigen plasmids. The SV40 T-antigen plasmid was used to increase channel expression. Transfected cells were identified visually using enhanced green fluorescent protein (eGFP) expression in the second cassette of the plasmid expressing the β_3 subunit. Whole-cell patch-clamp[82] was used to record Ca^{2+} currents at room temperature (23 ± 2 °C) 36–72 h after transfection. Data acquisition was performed using pCLAMP 9 (Molecular Devices) and an Axopatch 200B amplifier (Molecular Devices). Pipettes were pulled from borosilicate glass capillaries (TW150F-3; World Precision Instruments) and polished (MF-900 Microforge; Narishige) to obtain 2–3 MΩ resistances. 40–60% of the voltage error due to the series resistance was compensated, and leak currents were subtracted using a P/4 protocol. For $Ca_V1.2$ experiments, the pipette solution contained 120 mM NMDG, 1 mM $MgCl_2$, 5 mM EGTA, 4 mM Mg-ATP, 42 mM HEPES (pH 7.3 adjusted with methane sulfonic acid). The bath solution contained 40 mM $CaCl_2$, 1 mM $MgCl_2$, 105 mM Tris (pH 7.3 adjusted with methane sulfonic acid). Statistical significance was assessed using Student's *t*-tests or Mann–Whitney *U*-tests as appropriate.

Data quantification and statistical analysis

All of the details of data analysis and statistical analysis are provided in the Methods and the figure legends. All results are from at least two independent oocyte batches or two independent HEK293 transfections. Data were acquired using Clampex 11.2 (Molecular

Devices) and analysed with Clampfit 10.6 (Axon Instruments). Activation curves were obtained by fitting the data (GraphPad Prism) with the following Boltzmann equation: $Y = Y_{min} + (Y_{max} - Y_{min})/(1 + \exp((V_{1/2} - V_m)/k)$, where $V_{1/2}$ is the midpoint of activation, k is the slope factor of the activation curve, $Y = G/G_{max}$ and Y_{max} and Y_{min} are the maximum and minimum values of G/G_{max}, respectively, where $G = I/(V_m - E_{rev})$ and G_{max} is the maximal macroscopic conductance, where I is the measured peak current at each test potential (V_m). All data values are presented as mean ± s.e.m. n values represent the number of oocytes or number of cells. Statistical significance of the observed effects was assessed using unpaired t-tests using GraphPad Prism (v.9.3.1). $P < 0.01$ was considered to be significant, unless otherwise stated.

P values for Fig. 5c are as follows: $P = 0.0007$ ($Ca_V1.2(\Delta C)$), $P = 0.0321$ ($Ca_V1.2(\Delta C{:}3A)$–$Ca_V\beta_3$), $P = 0.0799$ ($Ca_V1.2(\Delta C)$–$Ca_V\beta_3(5A)$), $P = 0.0298$ ($Ca_V1.2(\Delta C)$–$Ca_V\beta_3(\Delta 220–240)$), P = 0.0028 ($Ca_V1.2(\Delta C)$–$Ca_V\beta_3(5A{:}\Delta 220–240)$), $P = 0.0019$ ($Ca_V1.2(\Delta C)$–$Ca_V\beta_3(11A)$), $P = 0.0028$ ($Ca_V1.2(\Delta C{:}3A)$–$Ca_V\beta_3(11A)$), $P < 0.0001$ ($Ca_V1.2(\Delta C)$–$Ca_V\beta_3$ *EMC5* knockout), $P = 0.0013$ ($Ca_V1.2(\Delta C)$–$Ca_V\beta_3$ *EMC6* knockout) and $P = 0.3513$ ($Cav1.2(\Delta C)$–$Cav\beta_{3(HEK293FT)}$).

Stain-free gel image analysis and in-gel digestions for MS analysis

Purified protein samples were diluted in 4× Laemmli Sample Buffer (Bio-Rad) containing 10% β-mercaptoethanol. The samples (1 μg of protein per well) were loaded onto a protein gel (BioRad, 4–15% Criterion TGX Stain-Free Precast Gel). Gels were run at 200 V for 42 min and imaged on a gel imager (BioRad, ChemiDoc MP) using the stain-free gel setting. Gels were stained with colloidal blue stain (Invitrogen) overnight at room temperature with gentle agitation. Excess stain was removed by briefly (3 min) rinsing the gel in de-stain solution (50% water, 40% methanol, 10% acetic acid) followed by three 15 min washes with MilliQ water. Gel lanes were cut into thirds. Each gel slice was subsequently diced into approximately 1 mm cubes. Gel cubes corresponding to a single gel slice were transferred to a 1.5 ml microcentrifuge tube (Protein Lo-Bind, Eppendorf). Ammonium bicarbonate (100 mM; ABC) was added to each tube (75 μl, or enough to completely cover gel cubes), and the samples were incubated for 10 min at room temperature. ABC solution was pipetted away with gel-loading tips (VWR). A total of 100 μl of 100 mM ABC and 10 μl of DTT (50 mM) was added to each sample before incubating at 55 °C (400 rpm, for 30 min). Excess buffer was removed with a gel-loading tip and replaced with 100 μl of 100 mM ABC and 10 μl of 150 mM iodoacetamide. The samples were incubated in the dark for 30 min at room temperature. Buffer was removed, and gel cubes were washed twice with 150 μl of 1:1 100 mM ABC:acetonitrile on a rotator at room temperature for 10 min. After the last wash, gel cubes were dehydrated with 100 μl of acetonitrile. Excess acetonitrile was removed using a speed-vac for 30 min. A total of 150 μl of 3.3 ng μl^{-1} trypsin (Promega) in ABC (50 mM) was added to each sample (0.5 μg trypsin per sample) and incubated on a shaker (300 rpm) at 37 °C for 16 h.

After digestion, the samples were acidified and peptides were eluted through the addition of 250 μl of a 66% acetonitrile, 33% ABC (100 mM), 1% formic acid solution. The samples were then centrifuged at 10,000*g* for 2 min, and the resulting supernatants were transferred

to new Protein LoBind tubes (Eppendorf). The peptide elution step was repeated and the corresponding supernatants were combined. The samples were then dried using a speed-vac for 2 h.

Crude dried peptides were cleaned using ZipTip C18 columns (Millipore) according to the manufacturer's instructions. In brief, peptides were resuspended in 20 µl of resuspension buffer (5:95 acetonitrile:MilliQ H_2O, 0.1% trifluoroacetic acid) and solubilized in a bath sonicator (VWR, 35 kHz, 10 min). A ZipTip was placed onto a P10 pipettor set to 10 µl, and the C18 column was activated twice with 10 µl of hydration buffer (50:50 acetonitrile:MilliQ H_2O, 0.1% trifluoroacetic acid), followed by a single wash step with 10 µl of wash buffer (0.1% trifluoroacetic acid in water). Peptides were loaded onto the C18 ZipTip column by taking up 10 µl of sample and slowly pipetting up and down 10 times. This loading step was repeated once more before washing twice with 10 µl of wash buffer. Finally, 10 µl of elution buffer (60:40 acetonitrile:MilliQ H_2O, 0.1% trifluoroacetic acid) was taken up into the ZipTip and expelled into a fresh LoBind tube, followed by pipetting up and down 10 times inside the tube. The elution step was repeated once. Eluted peptides were dried using the speed-vac for 20 min and then stored at −20 °C until MS analysis.

Before MS analysis, peptides were resuspended in loading buffer (2% acetonitrile, 0.1% formic acid) and completely solubilized in a bath sonicator (VWR, 35 kHz, 10 min).

MS acquisition and analysis

LC and timsTOF Pro.—A nanoElute (Bruker) was attached in line to a timsTOF Pro equipped with a CaptiveSpray Source (Bruker). Chromatography was conducted at 40 °C through a 25 cm reversed-phase C18 column (PepSep) at a constant flow-rate of 0.5 µl min^{-1}. Mobile phase A was 98/2/0.1% liquid chromatography (LC)–MS grade H_2O/acetonitrile/formic acid (v/v/v) and phase B was LC–MS-grade acetonitrile with 0.1% formic acid (v/v). During a 108-min method, peptides were separated by a three-step linear gradient (5% to 30% B over 90 min, 30% to 35% B over 10 min, 35% to 95% B over 4 min) followed by a 4-min isocratic flush at 95% before washing and a return to low organic conditions. Experiments were run as data-dependent acquisitions with ion mobility activated in PASEF mode. MS and MS/MS spectra were collected with m/z 100 to 1,700 and ions with $z = +1$ were excluded.

Raw data files were searched using PEAKS Online Xpro 1.6 (Bioinformatics Solutions). The precursor mass error tolerance and fragment mass error tolerance were set to 20 PPM and 0.05, respectively. The trypsin digest mode was set to semi-specific and missed cleavages was set to 3. The human Swiss-Prot reviewed (canonical) database (downloaded from UniProt) and the common repository of adventitious proteins (cRAP, downloaded from The Global Proteome Machine Organization) totalling 20,487 entries were used. Carbamidomethylation was selected as a fixed modification. Acetylation (N-term), deamidation (NQ) and oxidation (M) were selected as variable modifications. The maximum number of variable post translational modifications per peptide was 3.

All experiments were repeated in triplicate and the combined datasets were filtered using the following criteria: (1) all proteins from the common contaminants search database and

all keratins were removed; (2) required a protein to be found in all three replicates of at least one condition; (3) at least 20% coverage; (4) at least 4 peptides and 4 unique peptides; (5) median area of at least 25,000 across all 3 replicates in the $Ca_v1.2(\Delta C)$–$Ca_v\beta_3$ sample (denoted as Alpha+Beta in Supplementary Table 1).

Raw data files and searched datasets are available at the Mass Spectrometry Interactive Virtual Environment, a member of the Proteome Xchange consortium (https://massive.ucsd.edu/) under the identifier MSV000090434. The filtered dataset is also available in Supplementary Table 1.

Sample preparation and cryo-EM data acquisition

For cryo-EM, 3.5 μl of 1.7 mg ml^{-1} $Ca_v1.2(\Delta C)$–$Ca_v\beta_3$ sample or 2.7 mg ml^{-1} $Ca_v1.2(\Delta C)$–$Ca_v\beta_3$–$Ca_v\alpha_2\delta$ sample was applied to Quantifoil R1.2/1.3 300 mesh Au holey-carbon grids, blotted for 4–6 s at 4 °C and 100% humidity using a FEI Vitrobot Mark IV (Thermo Fisher Scientific) and plunge-frozen in liquid ethane. Cryo-EM grids were screened on the FEI Talos Arctica cryo-TEM system (Thermo Fisher Scientific) (at University of California, San Francisco (UCSF) EM Facility and SLAC National Accelerator Laboratory) operated at 200 kV and equipped with a K3 direct detector camera (Gatan), and then imaged on a 300 kV FEI Titan Krios microscope (Thermo Fisher Scientific) with a K3 direct detector camera (Gatan) (UCSF). Cryo-EM datasets were collected in super-resolution counting mode at a nominal magnification of ×105,000 with a super-resolution pixel size of 0.4233 Å (physical pixel size of 0.8466 Å) using SerialEM[83]. Images were recorded with a 2.024 s exposure over 81 frames with a dose rate of 0.57 e^- $Å^{-2}$ per frame. The defocus range was set from −0.9 μm to −1.7 μm.

Image processing and 3D reconstruction

A total of 14,341 and 13,704 movie stacks were collected for the $Ca_v1.2(\Delta C)$–$Ca_v\beta_3$ and $Ca_v1.2(\Delta C)$–$Ca_v\beta_3$–$Ca_v\alpha_2\delta$ samples, respectively. Initial image processing was performed in cryoSPARC-3.2 (ref. 84). Raw movies were motion-corrected by a factor of two (final pixel size of 0.8466 Å) using the patch motion correction program. Contrast transfer function parameters of the resulting micrographs were estimated using the patch CTF program in cryoSPARC-3.2. Particles were picked by blob picking, extracted using a box size of 440 Å. Particles were subsequently template picked with 2D class averages low-pass filtered to 20 Å and extracted using 440 Å box size. After several rounds of clean-up using reference-free 2D classification, an ab initio model was generated and heterogenous refinement was then performed without imposing any symmetry. Particles with reasonable 3D reconstructions (as judged by the Fourier shell correlation curve shapes) were processed for non-uniform refinement to archive 3D reconstructions with the highest resolution.

To improve the features of each 3D reconstruction, multibody refinement was performed in RELION-3.1 (ref. 85). For $Ca_V1.2$–$Ca_V\beta_3$, 239,729 refined particles were exported from cryoSPARC-3.2 to RELION-3.1 using the csparc2star.py (UCSF pyem v.0.5) suite of conversion scripts (https://doi.org/10.5281/zenodo.3576630). After 3D refinement in RELION-3.1 using the refined map from cryoSPARC-3.2 and the exported particles, an overall 3.4 Å EM density map was obtained (EMC:$Ca_v1.2$–$Ca_v\beta3$ (ECAB) map 1)

(processing flow charts are shown in Extended Data Fig. 1i). To improve the map features of the flexible regions, multibody refinement was performed in RELION-3.1 using two bodies: (1) body I containing the lumenal domain (that is, EMC1, EMC4, EMC7 and EMC10) and the transmembrane region ($Ca_V1.2$, EMC1 TM1, EMC3 TM1–3, EMC5 TM1–2 and EMC6) of ECAB map 1); and (2) body II containing the cytoplasmic domain ($Ca_V\beta_3$, EMC2, EMC8, and the cytoplasmic segments of EMC3 and EMC5) and an overlapping portion of the transmembrane region. The phenix.combine_focused_maps program was used to combine the two segments with improved features from multibody refinement[86]. A similar strategy was applied to 269,950 particles of ECAB map 2 to obtain a 3.6 Å consensus map, followed by feature improvement using multibody refinement in RELION-3.1. ECAB map 1 and ECAB map 2 (cross correlation = 0.9836) were merged using Phenix to obtain ECAB map 3 with the best features[86]. The pool of 269,802 particles of $Ca_v1.2$–$Ca_v\beta3$–$Ca_v\alpha2\delta$ (CABAD) map 1 was exported from cryoSPARC using the strategy as described above and processed for refinement in RELION-3.1, yielding a 3.3 Å consensus map. This map and particle set was further used to perform a two-body multibody refinement according to the procedure described above to obtain CABAD map 2.

Model building and refinement

ECAB map 3 and CABAD map 2 were used to build the model for the EMC–$Ca_v1.2(\Delta C)$–$Ca_v\beta_3$ complex and the $Ca_v1.2(\Delta C)$–$Ca_v\beta_3$–$Ca_v\alpha_2\delta$-1 complex, respectively. For the EMC–$Ca_v1.2(\Delta C)$–$Ca_v\beta_3$ complex, a preliminary model was built using the previously reported apo-EMC structure (Protein Data Bank (PDB): 6WW7)[29] and the $Ca_v\beta_3$ subunit in the $Ca_v2.2$ structure (PDB: 7MIY)[45]. For the $Ca_v1.2(\Delta C)$–$Ca_v\beta_3$–$Ca_v\alpha_2\delta$-1 complex, the $Ca_v2.2$ structure (PDB: 7MIY)[45] was used as starting model. Phyre2 server[87] was used to predict ten models of $Ca_v1.2$ using amino acid sequences (UniProt: Q13936–20) and, among them, the best model was selected by comparing them with the density map. The phenix.dock_in_map program was used to dock the models in respective maps[86]. As the density for $Ca_V\beta_3$ in the $Ca_v1.2(\Delta C)$–$Ca_V\beta_3$–$Ca_v\alpha_2\delta$-1 complex was weaker than for other parts of the channel, we rendered the $Ca_V\beta$ region of the $Ca_V1.2(\Delta C)$–$Ca_V\beta_3$–$Ca_V\alpha_2\delta$-1 complex at a threshold of 2.25 (>5 was used for the rest of map) and placed $Ca_V\beta_3$ from the de novo modelled EMC–$Ca_V1.2(\Delta C)$–$Ca_V\beta_3$ structure in the density, followed by rigid-body refinement of the $Ca_V1.2(\Delta C)$–$Ca_V\beta_3$–$Ca_V\alpha_2\delta$-1 complex. The docked model and maps were further manually checked and fitted in COOT[88]. Iterative structure refinement and model building were performed using the phenix.real_space_refine program[86]. The local resolution range for $Ca_v1.2$ was 2.0–4.8 Å (Supplementary Fig. 3e), which allowed model building by putting more emphasis on helix topology and large aromatic side-chain densities. However, model building was strictly performed on the basis of the available electron density. Restraint files necessary for refinement were generated using phenix.elbow[86,89]. Final statistics of 3D reconstruction and model refinement are provided in Extended Data Table 1. The per-residue B-factors, after final refinement against the overall map, were rendered on the refined model and are presented in Supplementary Fig. 3c–f. The final models were evaluated using MolProbity[90]. All figures and videos were generated using ChimeraX[91] and the Pymol package (http://www.pymol.org/pymol). Close-contact interaction analysis was performed using LIGPLOT and DIMPLOT[92,93].

Extended Data

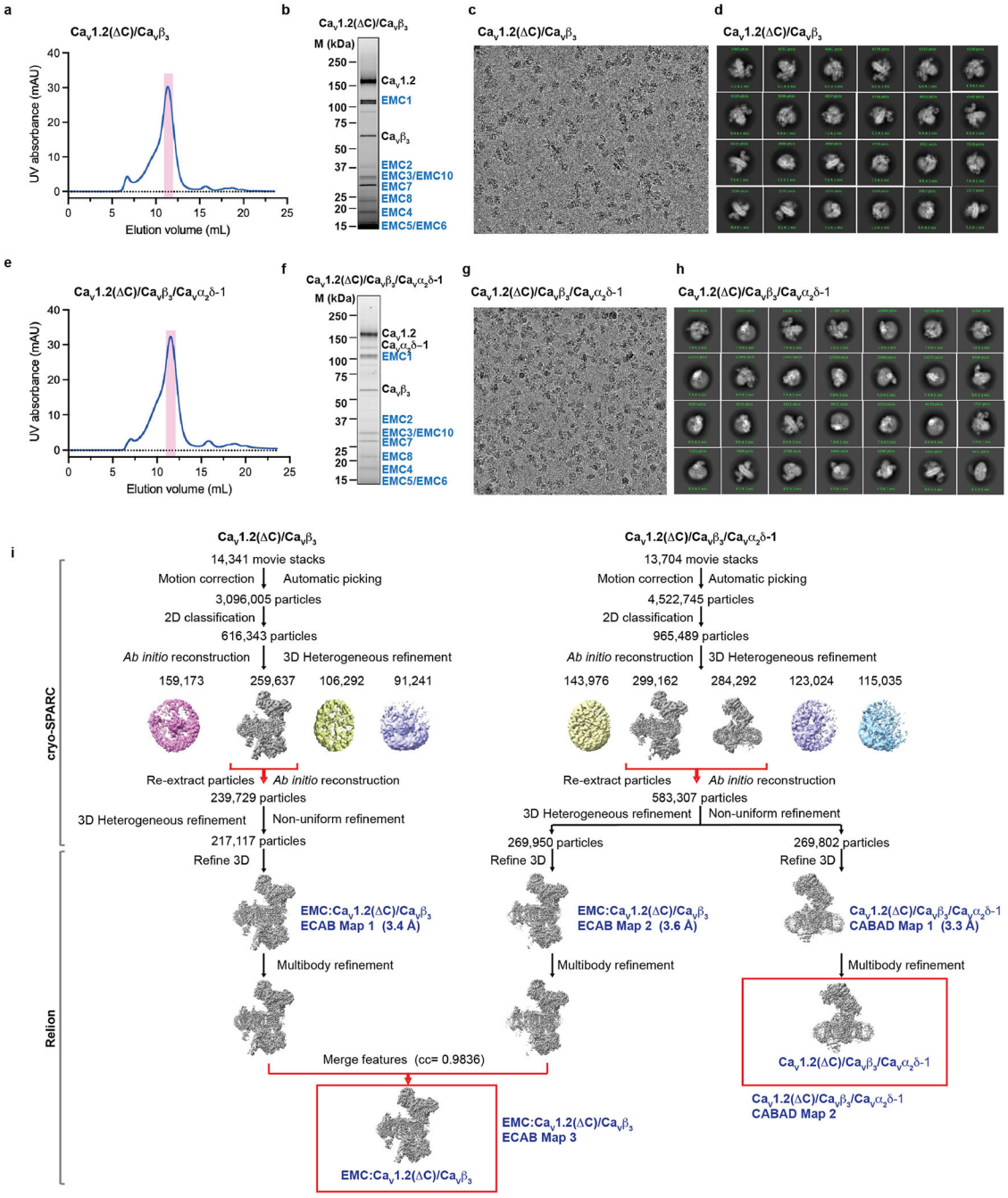

Extended Data Fig. 1 |. EMC:$Ca_V1.2(\Delta C)/Ca_V\beta_3$ and $Ca_V1.2(\Delta C)/Ca_V\beta_3/Ca_V\alpha_2\delta$-1 Cryo-EM analysis.

a-d, Exemplars of purified $Ca_V1.2(\Delta C)/Ca_V\beta_3$: **a**, SEC (Superose 6 Increase 10/300 GL). **b**, peak fraction SDS-PAGE. **c**, electron micrograph (~105,000x magnification), and **d**, 2D class averages. **e**–**h** Exemplars of purified $Ca_V1.2(\Delta C)/Ca_V\beta_3/Ca_V\alpha_2\delta$-1: **e**, SEC (Superose 6 Increase 10/300 GL). **f**, peak fraction SDS-PAGE. Magenta bars in 'a' and 'e' mark peak fraction. **g**, electron micrographs (~105,000x magnification), and

h, 2D class averages. **i**, Workflow for electron microscopy data processing for the $Ca_V1.2(\Delta C)/Ca_V\beta_3$ and $Ca_V1.2(\Delta C)/Ca_V\beta_3/Ca_V\alpha_2\delta$-1 samples. Initial cryoSPARC-3.2 *Ab initio* reconstruction identified a population of particles containing the EMC:$Ca_V1.2(\Delta C)/Ca_V\beta_3$ complex in the $Ca_V1.2(\Delta C)/Ca_V\beta_3$ sample and populations of particles containing either the EMC:$Ca_V1.2(\Delta C)/Ca_V\beta_3$ complex or $Ca_V1.2(\Delta C)/Ca_V\beta_3/Ca_V\alpha_2\delta$-1 complex in the $Ca_V1.2(\Delta C)/Ca_V\beta_3/Ca_V\alpha_2\delta$-1 sample. Red arrows indicate the three classes that were re-extracted, subjected to multiple rounds of 3D heterogeneous classification, and exported from cryoSPARC-3.2 for further 3D refinement in RELION-3.1. This resulted in two maps for the EMC:$Ca_V1.2(\Delta C)/Ca_V\beta_3$ complex (ECAB Maps 1 and 2) and one for the $Ca_V1.2(\Delta C)/Ca_V\beta_3/Ca_V\alpha_2\delta$-1 complex (CABAD Map 1). Multibody refinement was performed in RELION-3.1 to improve the features of flexible regions of the three maps. This resulted in the final map for the $Ca_V1.2(\Delta C)/Ca_V\beta_3/Ca_V\alpha_2\delta$-1 complex (CABAD Map 2). ECAB Maps 1–2 with improved flexible features were merged (cross correlation = 0.9836) to obtain the final map for the EMC:$Ca_V1.2(\Delta C)/Ca_V\beta_3$ complex (ECAB Map 3). Red boxes indicate the final maps used for model building. For ‘b-c’, N = 3. For ‘f-g’, N = 2.

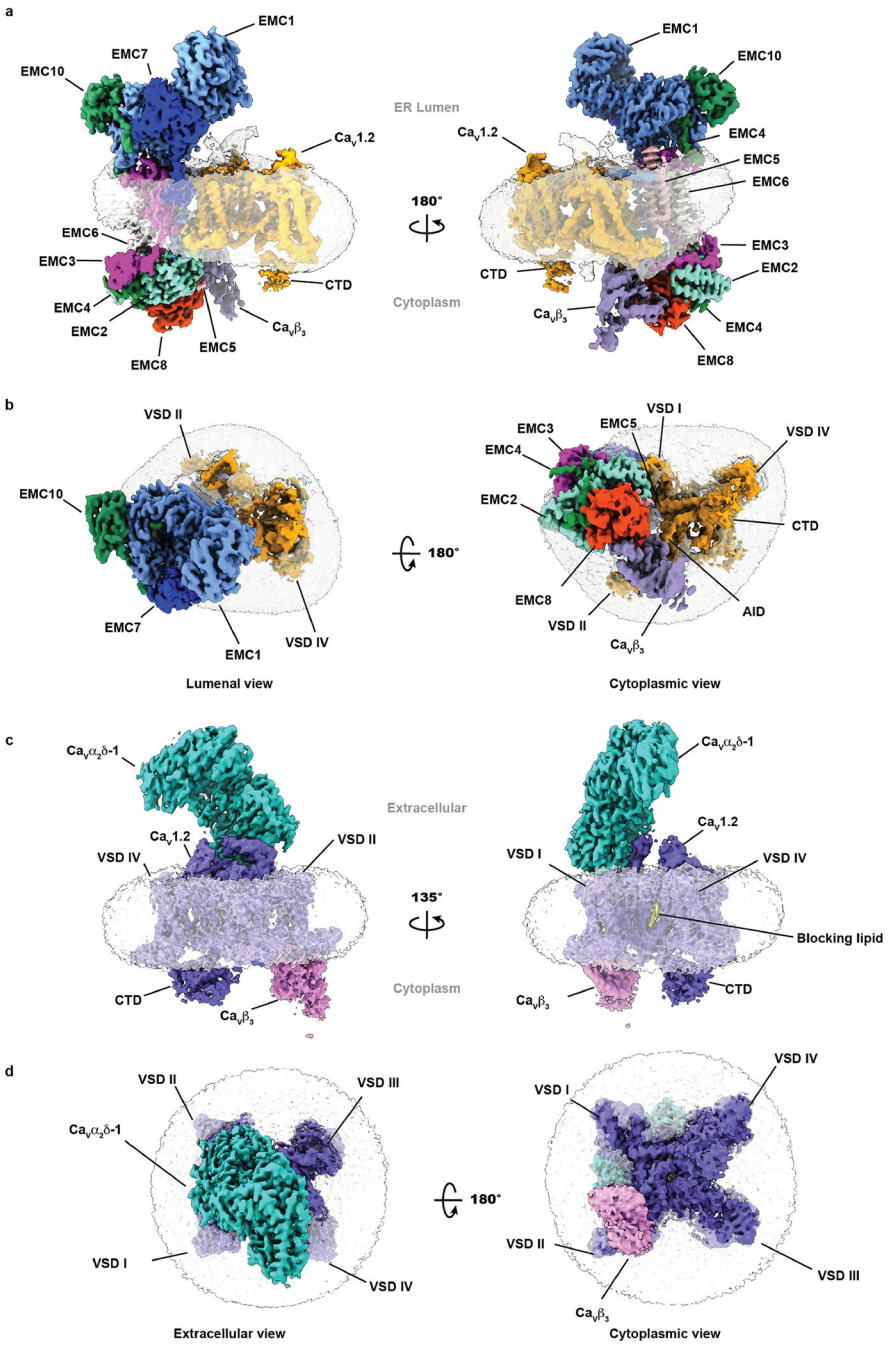

Extended Data Fig. 2 |. Cryo-EM maps of EMC:$Ca_V1.2$(ΔC)/$Ca_V\beta_3$ and $Ca_V1.2$(ΔC)/$Ca_V\beta_3$/$Ca_V\alpha_2\delta$-1 complexes.

EMC:$Ca_V1.2$(ΔC)/$Ca_V\beta_3$ complex **a**, side views and **b**, lumenal (left) and cytoplasmic (right) views. Subunits are coloured as: EMC1 (light blue), EMC2 (aquamarine), EMC3 (light magenta), EMC4 (Forest), EMC5 (light pink), EMC6 (white), EMC7 (marine), EMC8 (orange), EMC10 (smudge), $Ca_V1.2$ (bright orange), and $Ca_V\beta_3$ (lavender). $Ca_V1.2$(ΔC)/$Ca_V\beta_3$/$Ca_V\alpha_2\delta$-1 **c**, side views and **d**, extracellular (left) and cytoplasmic (right) views. Subunits are coloured as: $Ca_V1.2$ (slate), $Ca_V\beta_3$ (violet), and $Ca_V\alpha_2\delta$-1 (greencyan). Detergent micelle is clear.

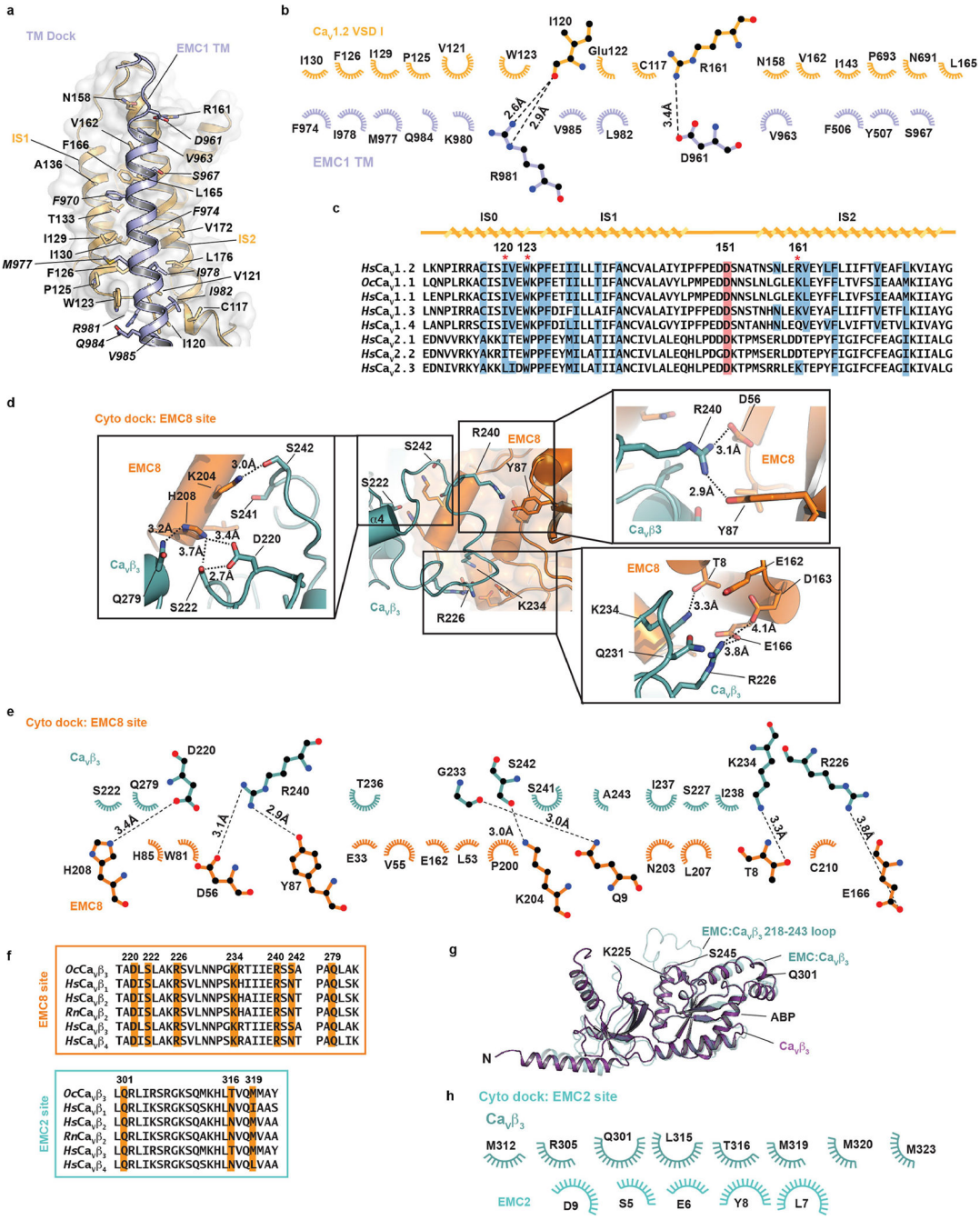

Extended Data Fig. 3 |. EMC:Ca$_V$1.2(ΔC)/Ca$_V$β$_3$ binding sites.

a, View of the TM dock interaction. EMC1 TM1 (slate) and Ca$_V$1.2 VSD I (yellow orange) interface. Interface buries 1051 Å^2. Select elements and residues are indicated. EMC1 residues are in italics. **b**, LigPLOT[92] diagram of EMC1 TM:Ca$_V$1.2 VSD I interactions showing ionic interactions (dashed lines) and van der Waals contacts ≤ 5Å. **c**, Sequence comparison of the indicated VSDI sequences for human Ca$_V$1.2 (*Hs*Ca$_V$1.2 (109–182)) (Uniprot Q13936–20) with rabbit Ca$_V$1.1 (*Oc*Ca$_V$1.1 (36–109)) (NCBI: NP_001095190.1), and human L-type (*Hs*Ca$_V$1.1 (36–109), *Hs*Ca$_V$1.3 (111–184), and *Hs*Ca$_V$1.4 (77–150))

(NCBI: NP_000060.2, NP_000711.1, and NP_005174.2) and non-L-Type (*Hs*$Ca_V2.1$ (83–156), *Hs*$Ca_V2.2$ (80–153), and *Hs*$Ca_V2.3$ (74–147)) (NCBI: NP_000059.3, NP_000709.1, and NP_001192222.1) channels. Red asterisks indicate residues involved in the cation-π pocket (120 and 123) and salt bridge (161). Red band highlights the residue that coordinates the Ca^{2+} ion in the $Ca_V\alpha_2\delta$ VWA domain. **d**, $Ca_V\beta_3$:EMC8 interaction. Callouts show the details of the indicated parts of the $Ca_V\beta_3$ NK loop interaction with EMC8. **e**, LigPLOT[92] diagram of $Ca_V\beta_3$:EMC8 interactions showing ionic interactions (dashed lines) and van der Waals contacts ≤ 5Å. $Ca_V\beta$:*EMC*8 hydrogen bond and salt bridge pairs are: Asp220:*His208*, Ser222:*His208*, Arg226:*Glu166*, Lys234:*Thr8*, Arg240:*Asp56/Tyr87*, Ser242:*Lys204*, and Gln279: *His208*. **f**, Sequence conservation for the indicated $Ca_V\beta$ elements from the EMC8 (top) and EMC2 (bottom) interaction sites. *Oc*$Ca_V\beta_3$ (Uniprot P54286; 218–243, 277–282; 300–322); *Hs*$Ca_V\beta_1$ (Uniprot Q02641.3; 270–295, 329–334; 352–374); *Hs*$Ca_V\beta_2$ (Uniprot Q08289; 322–347, 381–386; 404–426); *Rn*$Ca_V\beta_2$ (Uniprot Q8VGC3; 318–343, 377–382; 400–422); *Hs*$Ca_V\beta_3$ (Uniprot P54284; 218–243, 277–282; 300–322); *Hs*$Ca_V\beta_4$ (Uniprot O00305; 260–285, 319–324; 342–364). **g**, Superposition of rat $Ca_V\beta_3$ alone (violet, PDB:1VYU, chain B[39]) and $Ca_V\beta_3$ from the EMC complex. Boundaries of the disordered part of the T218-A243 loop in $Ca_V\beta_3$, and Q301, and ABP, are indicated, ($RMSD_{C\alpha}$ = 1.39Å). **h**, LigPLOT[92] diagram of $Ca_V\beta_3$:EMC2 interactions showing van der Waals contacts ≤ 5Å.

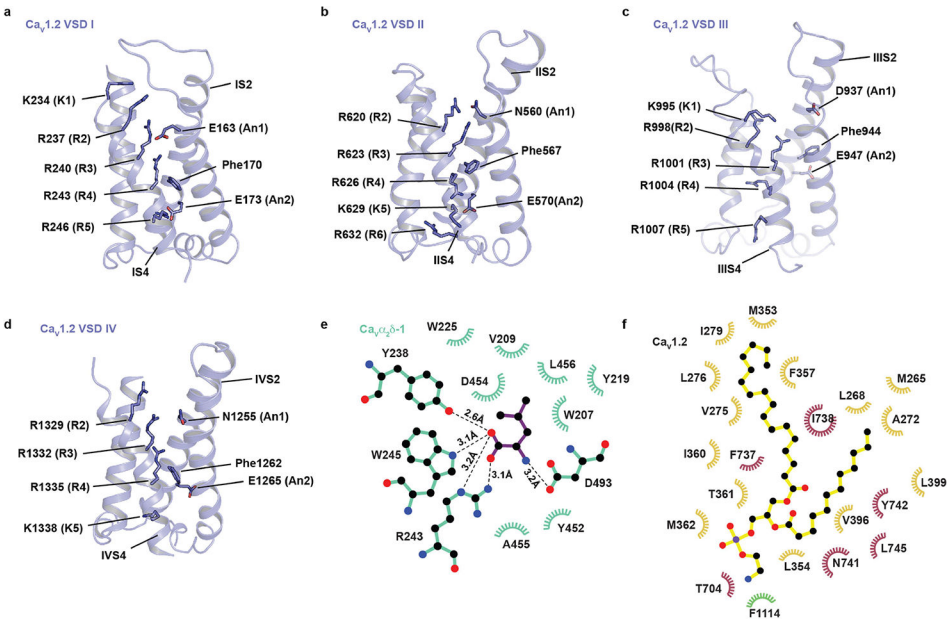

Extended Data Fig. 4 |. $Ca_V1.2$ structural details.

a–**d**, Structures of the indicated VSDs from the $Ca_V1.2(\Delta C)/Ca_V\beta_3/Ca_V\alpha_2\delta$-1 complex. Gating charge residues, anionic counter charges (An1 and An2) and aromatic site of the charge transfer centre[43,45,55] are shown. **e**, LigPLOT[92] diagram of the $Ca_V\alpha_2\delta$-1 leucine binding site showing hydrogen bonds and ionic interactions (dashed lines) and van der Waals contacts ≤ 5Å. **f**, LigPLOT[92] diagram of blocking lipid: $Ca_V1.2$ showing van der Waals contacts ≤ 5Å. Domain I (yellow orange), Domain II (dark red), and Domain III (green) residues are indicated.

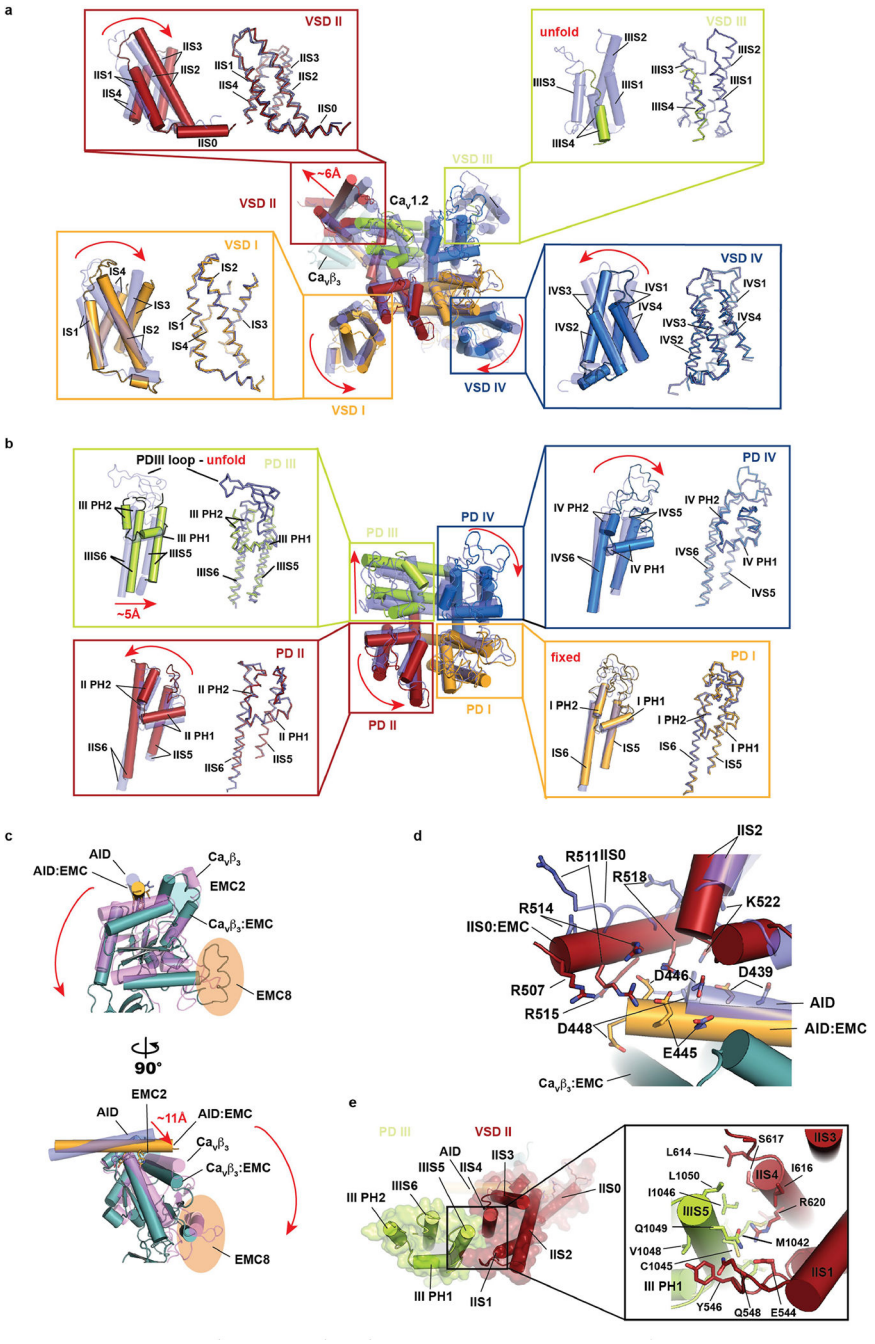

Extended Data Fig. 5 |. Conformational changes between EMC-bound and $Ca_V\alpha_2\delta$-bound $Ca_V1.2(\Delta C)/Ca_V\beta_3$.

Superposition of $Ca_V1.2$ from the EMC:$Ca_V1.2(\Delta C)/Ca_V\beta_3$ and $Ca_V1.2(\Delta C)/Ca_V\beta_3$/$Ca_V\alpha_2\delta$-1 complexes showing **a**, VSD conformational changes. **b**, PD conformational changes showing the superposition from 'a'. Insets show each PD. Elements $Ca_V1.2$ from the EMC complex are: VSD I/PD I (yellow orange), VSD II/PD II (firebrick), VSD III/PD III (lime), VSD IV/PD IV (marine). $Ca_V1.2$ (slate) and $Ca_V\beta_3$ (violet) from $Ca_V1.2(\Delta C)/Ca_V\beta_3/Ca_V\alpha_2\delta$-1 and $Ca_V\beta_3$ from the EMC (light teal) are semi-transparent. **c**, Superposition of $Ca_V\beta_3$ and the $Ca_V1.2$ AID helix from the EMC:$Ca_V1.2(\Delta C)/Ca_V\beta_3$

and $Ca_V1.2(\Delta C)/Ca_V\beta_3/Ca_V\alpha_2\delta$-1 complexes. Location of EMC8 is indicated by the orange oval. Red arrows in 'a-c' indicate conformational changes between $Ca_V1.2(\Delta C)/Ca_V\beta_3/Ca_V\alpha_2\delta$-1 and EMC:$Ca_V1.2(\Delta C)/Ca_V\beta_3$. **d**, Comparison of IIS0 and surrounding regions in the EMC complex (VSDII, firebrick; AID (yellow orange), and $Ca_V\beta_3$ (light teal)) their corresponding elements in $Ca_V1.2(\Delta C)/Ca_V\beta_3/Ca_V\alpha_2\delta$-1 (slate). **e**, Interactions between VSD II:PD III in the $Ca_V\beta$:AID:VSD II: PD III subcomplex from the EMC:$Ca_V1.2(\Delta C)/Ca_V\beta_3$ structure.

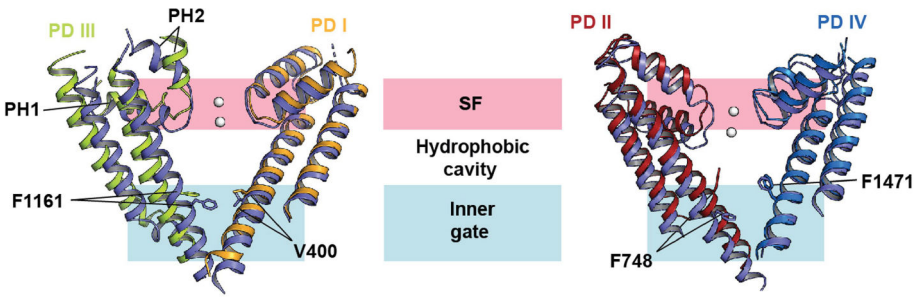

Extended Data Fig. 6 |. $Ca_V1.2$ pore domain superposition for EMC-bound and $Ca_V\alpha_2\delta$-bound $Ca_V1.2(\Delta C)/Ca_V\beta_3$.

Pore domains from the EMC-bound complex are: PD I (yellow orange), PD II (firebrick), PD III (lime), and PD IV (marine). Pore domains from $Ca_V1.2(\Delta C)/Ca_V\beta_3/Ca_V\alpha_2\delta$-1 are slate. Calcium ions are from $Ca_V1.2(\Delta C)/Ca_V\beta_3/Ca_V\alpha_2\delta$-1. Selectivity filter (SF), hydrophobic cavity, and inner gate regions and select residues are indicated.

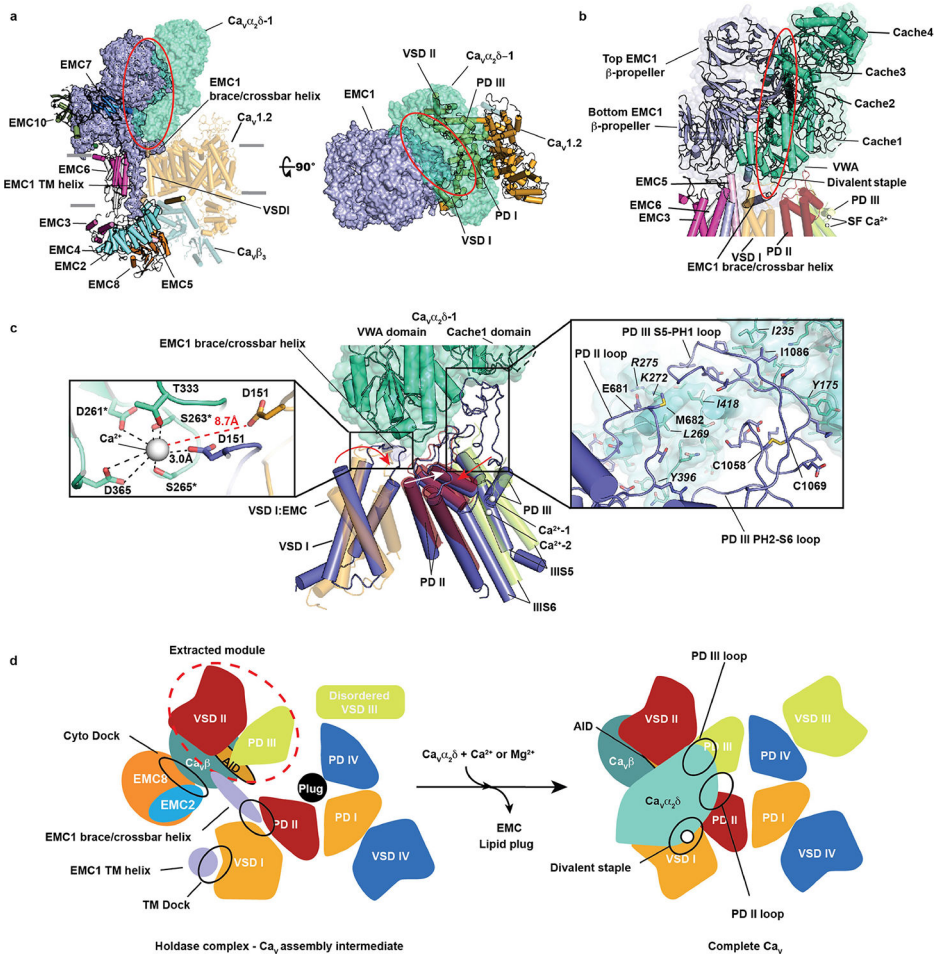

Extended Data Fig. 7 |. Mutually exclusive interactions of the EMC holdase and $Ca_V\alpha_2\delta$ with the core $Ca_V1.2/Ca_V\beta_3$ complex and ordering of the $Ca_V1.2$ pore and VSDs by $Ca_V\alpha_2\delta$.

a, Superposition of $Ca_V\alpha_2\delta$-1 (semi-transparent, aquamarine) from the $Ca_V1.2(\Delta C)/Ca_V\beta_3/Ca_V\alpha_2\delta$-1 structure with the EMC:$Ca_V1.2/Ca_V\beta_3$ complex. EMC1 surface is shown. Red oval highlights clash regions. Colours of the EMC:$Ca_V1.2/Ca_V\beta_3$ complex are as in Fig. 1a. Grey bars denote the membrane. **b**, Close up view of clash between EMC1 (light blue) and $Ca_V\alpha_2\delta$-1 (aquamarine). EMC1, EMC3 (magenta), EMC5 (pink), EMC6 (white), VSD I (yellow orange), PD II (firebrick), and PD III (lime) from the EMC:$Ca_V1.2/Ca_V\beta_3$ complex are shown. Red oval highlights clash regions. $Ca_V\alpha_2\delta$-1 domains are indicated. Divalent staple is indicated. SF calcium ions are from $Ca_V1.2(\Delta C)/Ca_V\beta_3/Ca_V\alpha_2\delta$-1 and mark the location of the pore in the $Ca_V\alpha_2\delta$-assembled channel. **c**, Superposition of VSD I (yellow orange), PD II (firebrick), and PD III (lime) from the EMC complex (semi-transparent) and their corresponding parts from $Ca_V1.2(\Delta C)/Ca_V\beta_3/Ca_V\alpha_2\delta$-1 (slate). $Ca_V\alpha_2\delta$-1 (aquamarine) is shown as a semi-transparent surface. Calcium ions are from $Ca_V1.2(\Delta C)/Ca_V\beta_3/Ca_V\alpha_2\delta$-1. Left inset shows the coordination of the divalent staple by the VWA domain MIDAS and D151 in $Ca_V1.2(\Delta C)/Ca_V\beta_3/Ca_V\alpha_2\delta$-1. Red distance shows the position of $Ca_V1.2$ D151 in the EMC complex relative to the calcium ion in the $Ca_V\alpha_2\delta$ complex. Asterisks mark positions where coordinated alanine mutation impair the ability of $Ca_V\alpha_2\delta$ to enhance Ca_V currents and surface expression[59]. Right inset shows the extensive

contacts between PD II and PD III loops with $Ca_V\alpha_2\delta$ in the $Ca_V1.2(\Delta C)/Ca_V\beta_3/Ca_V\alpha_2\delta$-1 complex. The PD III loops are disordered in the EMC:$Ca_V1.2/Ca_V\beta_3$ complex. $Ca_V\alpha_2\delta$-1 residues are in italics. **d**, Schematic showing of the conformational changes and interaction sites in the exchange between the EMC:$Ca_V/Ca_V\beta$ holdase complex and assembled $Ca_V/Ca_V\beta/Ca_V\alpha_2\delta$ channel. Black ovals indicate key interaction sites in each complex.

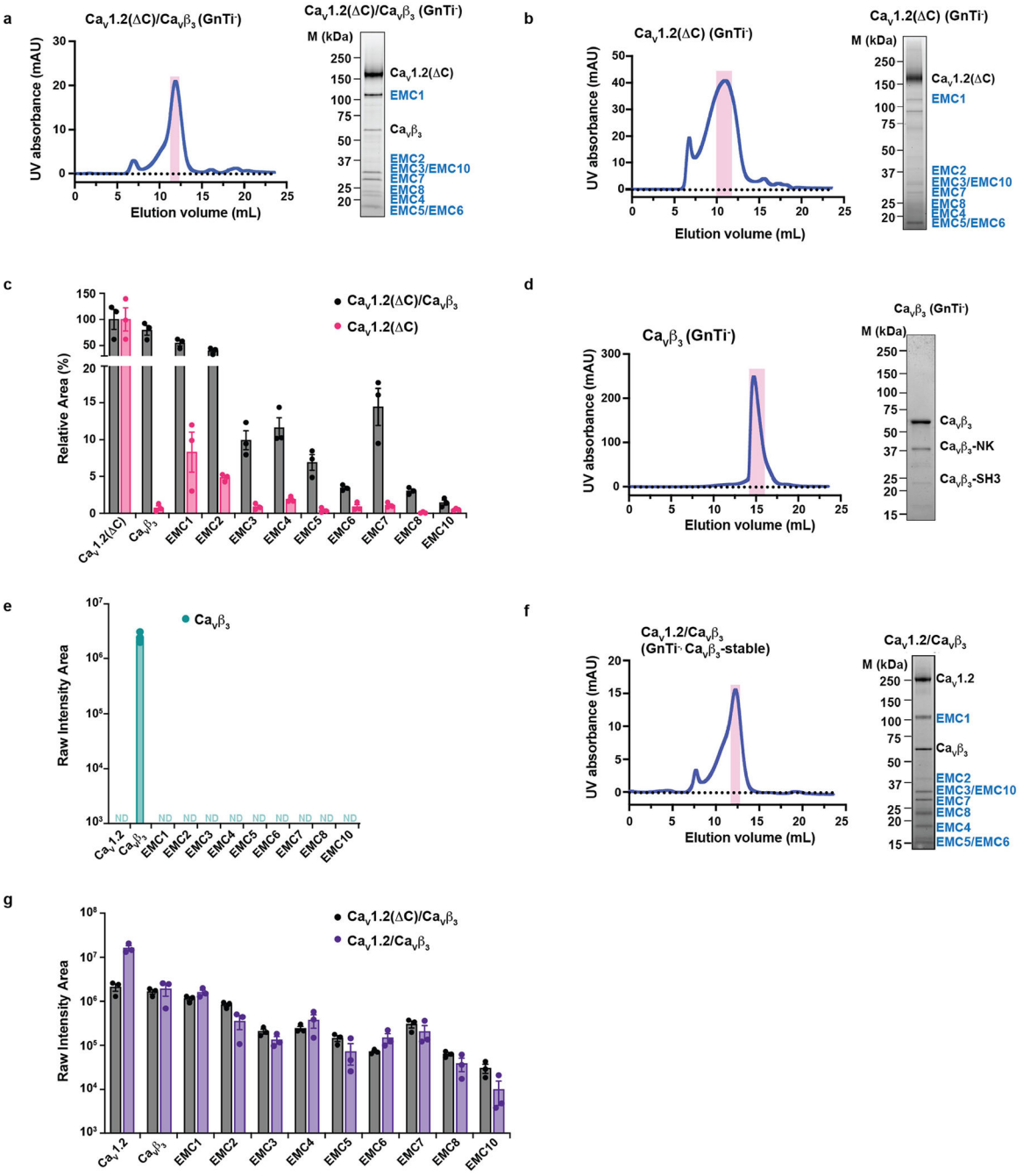

Extended Data Fig. 8 |. Exemplar purification of Ca_V subunit combinations.

a-c Superose 6 Increase 10/300 GL chromatogram and peak fraction SDS-PAGE for: **a**, $Ca_V1.2(\Delta C)/Ca_V\beta_3$ and **b**, $Ca_V1.2(\Delta C)$. **c**, Relative detection by mass spectrometry from

'a' and 'b' of EMC proteins with respect to $Ca_V1.2(\Delta C)$ across 3 replicates. **d**, Superose 6 Increase 10/300 GL chromatogram and peak fraction SDS-PAGE for $Ca_V\beta_3$. $Ca_V\beta_3$-NK and $Ca_V\beta_3$-SH3 are $Ca_V\beta_3$ proteolytic fragments. **e**, Absolute detection of EMC proteins and $Ca_V\beta_3$ by mass spectrometry following expression and purification of $Ca_V\beta_3$. **f**, Superose 6 Increase 10/300 GL chromatogram and peak fraction SDS-PAGE for $Ca_V1.2/Ca_V\beta_3$. Magenta bars in 'a' 'b', 'd', and 'f' mark peak fraction. **g**, Absolute detection of $Ca_V1.2$, $Ca_V1.2(\Delta C)$, $Ca_V\beta_3$, and EMC proteins from 'a' and 'f'. Error bars are calculated as SEM. ND denotes not detected.

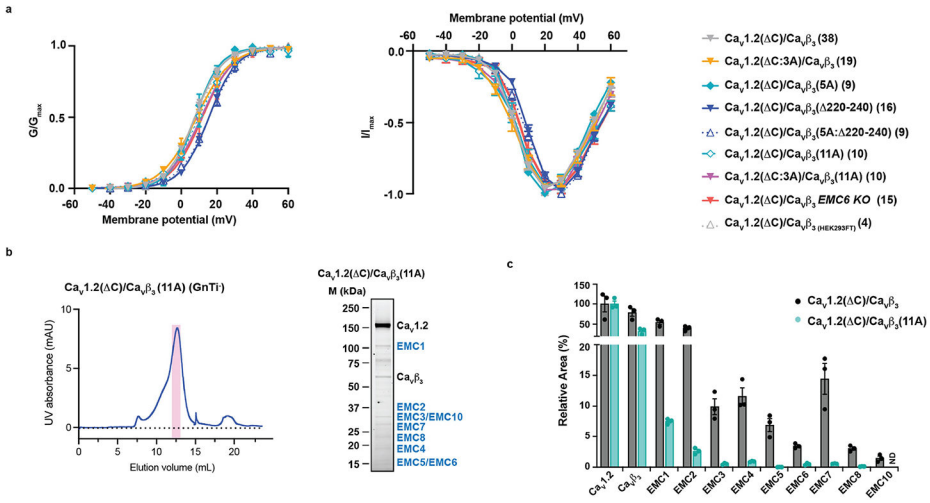

Extended Data Fig. 9 |. Functional and biochemical characterization of Ca_V mutants.
a, Voltage dependent activation (left) and I-V relationships (right) for the indicated channels. Parentheses indicate 'n' independent cells examined over >2 independent experiments. **b**, Superose 6 Increase 10/300 GL chromatogram and peak fraction SDS-PAGE for $Ca_V1.2(\Delta C)/Ca_V\beta_3(11A)$. Magenta bar marks peak fraction. **c**, Relative detection by mass spectrometry from 'b' of EMC proteins with respect to $Ca_V1.2(\Delta C)$ across 3 replicates. Data for $Ca_V1.2(\Delta C)/Ca_V\beta_3$ are from Extended Data Fig. 8c. 'ND' indicates 'not detected. Data in 'a' and 'c' are presented as mean ± SEM.

Extended Data Table 1 |

Statistics for data collection, refinement, and validation

	Cav1.2(ΔC)/Cavβ$_3$	Cav1.2(ΔC)/Cavβ$_3$/Cavα$_2$δ-1
Data collection and processing		
Magnification	105,000	105,000
Voltage (kV)	300	300
Electron dose (e−/Å^2)	46	46
Defocus range (μm)	−0.9~−1.7	−0.9~−1.7
Pixel size (Å)	0.8466	0.8466
Symmetry	C1	C1
Initial particle images (no.)	3,096,005	4,522,745

	Cav1.2(ΔC)/Cavβ$_3$	**Cav1.2(ΔC)/Cavβ$_3$/Cavα$_2$δ-1**	
Final particle images (no.)	217,117	269,950	269,802
Map resolution (Å)	3.4	3.6	3.3
FSC threshold	0.143	0.143	0.143
Map resolution range (Å)	3.0~8.0	3.0~8.0	2.0~4.8
Refinement	ECAB Map 3 **(PDB:8EOI;EMD-28376)**		CABAD Map 2 **(PDB:8EOG;EMD-28375)**
Initial model used (PDB code)	6WW7, 7MIY		7MIY
Model resolution (Å)	3.4		3.5
FSC threshold	0.5		0.5
Map sharpening *B* factor (Å^2)	−27.6		−82.1
Model composition			
Non-hydrogen atoms	28,721		19,729
Protein residues	3,562		2,416
Ligands	8		22
B factors (Å^2)			
Protein	176.18		129.67
Ligand	105.71		103.42
R.m.s deviations			
Bond lengths (Å)	0.002		0.003
Bond angles (°)	0.494		0.570
Validation			
MolProbity score	2.14		2.06
Clashscore	8.09		11.79
Poor rotamers (%)	2.73		0.51
Ramachandran plot			
Favored (%)	94.6		92.36
Allowed (%)	5.4		7.5
Disallowed (%)	0.03		0.13

Supplementary Material

Refer to Web version on PubMed Central for supplementary material.

Acknowledgements

We thank T.-J. Yen, D. Bulkley, Y. Liu and H. Khant for technical help; T. Pleiner and R. Vorhees for the HEK293FT cells and *EMC5*-knockout and *EMC6*-knockout lines; and K. Brejc, H. M. Colecraft, D. Julius and G. Thiel for comments on the manuscript. This work was supported by grants NIH R01 HL080050 and NIH R01 DC007664 to D.L.M.; the Beckman Foundation to B.W.Z.; the National Science Foundation GRFP DGE-2034836 to J.L.M.; and an American Heart Association postdoctoral fellowship to F.A.-A. B.W.Z. is a Beckman Young Investigator. Some of this work was performed at the Stanford-SLAC Cryo-EM Center (S^{2}C^2), which is supported by the National Institutes of Health Common Fund Transformative High-Resolution Cryo-Electron Microscopy program (U24 GM129541). The content is solely the responsibility of the authors and does not necessarily represent the official views of the National Institutes of Health.

Data availability

Coordinates and maps of the EMC–$Ca_V1.2(\Delta C)$–$Ca_V\beta_3$ complex (PDB: 8EOI; Electron Microscopy Data Bank (EMDB): EMD-28376, EMD-28578, EMD-28579,EMD-40559, EMD-40560)and $Ca_V1.2(\Delta C)$–$Ca_V\beta_3$–$Ca_V\alpha_2\delta$-1 complex (PDB: 8EOG; EMDB: EMD-28375, EMD-28561, EMD-28564, EMD-40561) have been deposited at the at the PDB and EMDB. MS data have been deposited at the Mass Spectrometry Interactive Virtual Environment (https://massive.ucsd.edu/) under identifier MSV000090434. Source data are provided with this paper.

References

1. Catterall WA, Wisedchaisri G & Zheng N The chemical basis for electrical signaling. Nat. Chem. Biol. 13, 455–463 (2017). [PubMed: 28406893]
2. Isacoff EY, Jan LY & Minor DL Jr. Conduits of life's spark: a perspective on ion channel research since the birth of neuron. Neuron 80, 658–674 (2013). [PubMed: 24183018]
3. Zamponi GW, Striessnig J, Koschak A & Dolphin AC The physiology, pathology, and pharmacology of voltage-gated calcium channels and their future therapeutic potential. Pharmacol. Rev. 67, 821–870 (2015). [PubMed: 26362469]
4. Nanou E & Catterall WA Calcium channels, synaptic plasticity, and neuropsychiatric disease. Neuron 98, 466–481 (2018). [PubMed: 29723500]
5. Buraei Z & Yang J The β subunit of voltage-gated Ca^{2+} channels. Physiol. Rev. 90, 1461–1506 (2010). [PubMed: 20959621]
6. Dooley DJ, Taylor CP, Donevan S & Feltner D Ca^{2+} channel $\alpha_2\delta$ ligands: novel modulators of neurotransmission. Trends Pharmacol. Sci. 28, 75–82 (2007). [PubMed: 17222465]
7. Dolphin AC Voltage-gated calcium channels and their auxiliary subunits: physiology and pathophysiology and pharmacology. J. Physiol. 594, 5369–5390 (2016). [PubMed: 27273705]
8. Jonikas MC et al. Comprehensive characterization of genes required for protein folding in the endoplasmic reticulum. Science 323, 1693–1697 (2009). [PubMed: 19325107]
9. Hegde RS The function, structure, and origins of the ER membrane protein complex. Annu. Rev. Biochem. 91, 651–678 (2022). [PubMed: 35287476]
10. Shistik E, Ivanina T, Puri T, Hosey M & Dascal N Ca^{2+} current enhancement by α_2/δ and β subunits in *Xenopus* oocytes: contribution of changes in channel gating and α1 protein level. J. Physiol. 489, 55–62 (1995). [PubMed: 8583415]
11. Singer D et al. The roles of the subunits in the function of the calcium channel. Science 253, 1553–1557 (1991). [PubMed: 1716787]
12. Gurnett CA, De Waard M & Campbell KP Dual function of the voltage-dependent Ca^{2+} channel $\alpha_2\delta$ subunit in current stimulation and subunit interaction. Neuron 16, 431–440 (1996). [PubMed: 8789958]
13. Davies A et al. Functional biology of the $\alpha_2\delta$ subunits of voltage-gated calcium channels. Trends Pharmacol. Sci. 28, 220–228 (2007). [PubMed: 17403543]
14. Field MJ et al. Identification of the α_2-δ-1 subunit of voltage-dependent calcium channels as a molecular target for pain mediating the analgesic actions of pregabalin. Proc. Natl Acad. Sci. USA 103, 17537–17542 (2006). [PubMed: 17088553]
15. Dolphin AC Voltage-gated calcium channel α2δ subunits: an assessment of proposed novel roles. F1000Res 10.12688/f1000research.16104.1 (2018).
16. Bauer CS et al. The increased trafficking of the calcium channel subunit $\alpha_2\delta$-1 to presynaptic terminals in neuropathic pain is inhibited by the α2δ ligand pregabalin. J. Neurosci. 29, 4076–4088 (2009). [PubMed: 19339603]
17. Cassidy JS, Ferron L, Kadurin I, Pratt WS & Dolphin AC Functional exofacially tagged N-type calcium channels elucidate the interaction with auxiliary $\alpha_2\delta$-1 subunits. Proc. Natl Acad. Sci. USA 111, 8979–8984 (2014). [PubMed: 24889613]

18. Deutsch C The birth of a channel. Neuron 40, 265–276 (2003). [PubMed: 14556708]
19. Christianson JC et al. Defining human ERAD networks through an integrative mapping strategy. Nat. Cell Biol. 14, 93–105 (2011). [PubMed: 22119785]
20. Guna A, Volkmar N, Christianson JC & Hegde RS The ER membrane protein complex is a transmembrane domain insertase. Science 359, 470–473 (2018). [PubMed: 29242231]
21. Richard M, Boulin T, Robert VJ, Richmond JE & Bessereau JL Biosynthesis of ionotropic acetylcholine receptors requires the evolutionarily conserved ER membrane complex. Proc. Natl Acad. Sci. USA 110, E1055–E1063 (2013). [PubMed: 23431131]
22. Talbot BE, Vandorpe DH, Stotter BR, Alper SL & Schlondorff JS Transmembrane insertases and *N*-glycosylation critically determine synthesis, trafficking, and activity of the nonselective cation channel TRPC6. J. Biol. Chem. 294, 12655–12669 (2019). [PubMed: 31266804]
23. Coelho JPL et al. A network of chaperones prevents and detects failures in membrane protein lipid bilayer integration. Nat. Commun. 10, 672 (2019). [PubMed: 30737405]
24. Satoh T, Ohba A, Liu Z, Inagaki T & Satoh AK dPob/EMC is essential for biosynthesis of rhodopsin and other multi-pass membrane proteins in *Drosophila* photoreceptors. eLife 4, e06306 (2015). [PubMed: 25715730]
25. Chitwood PJ, Juszkiewicz S, Guna A, Shao S & Hegde RS EMC is required to initiate accurate membrane protein topogenesis. Cell 175, 1507–1519 (2018). [PubMed: 30415835]
26. Miller-Vedam LE et al. Structural and mechanistic basis of the EMC-dependent biogenesis of distinct transmembrane clients. eLife 9, e62611 (2020). [PubMed: 33236988]
27. Shurtleff MJ et al. The ER membrane protein complex interacts cotranslationally to enable biogenesis of multipass membrane proteins. eLife 7, e37018 (2018). [PubMed: 29809151]
28. O'Donnell JP et al. The architecture of EMC reveals a path for membrane protein insertion. eLife 9, e57887 (2020). [PubMed: 32459176]
29. Pleiner T et al. Structural basis for membrane insertion by the human ER membrane protein complex. Science 369, 433–436 (2020). [PubMed: 32439656]
30. Bagchi P, Inoue T & Tsai B EMC1-dependent stabilization drives membrane penetration of a partially destabilized non-enveloped virus. eLife 5, e21470 (2016). [PubMed: 28012275]
31. Hofmann F, Flockerzi V, Kahl S & Wegener JW L-type $Ca_V1.2$ calcium channels: from in vitro findings to in vivo function. Physiol. Rev. 94, 303–326 (2014). [PubMed: 24382889]
32. Hullin R et al. Cardiac L-type calcium channel β-subunits expressed in human heart have differential effects on single channel characteristics. J. Biol. Chem. 278, 21623–21630 (2003). [PubMed: 12606548]
33. Zamponi GW Targeting voltage-gated calcium channels in neurological and psychiatric diseases. Nat. Rev. Drug Discov. 15, 19–34 (2016). [PubMed: 26542451]
34. Marcantoni A, Calorio C, Hidisoglu E, Chiantia G & Carbone E $Ca_v1.2$ channelopathies causing autism: new hallmarks on Timothy syndrome. Pflugers Arch. 472, 775–789 (2020). [PubMed: 32621084]
35. Chen Z, Mondal A & Minor DL Jr. Structural basis for $Ca_V\alpha_2\delta$:gabapentin binding. Nat. Struct. Mol. Biol. 10.1038/s41594-023-00951-7 (2023).
36. Kozai D et al. Recognition mechanism of a novel gabapentinoid drug, mirogabalin, for recombinant human $\alpha_2\delta1$, a voltage-gated calcium channel subunit. J. Mol. Biol. 435, 168049 (2023). [PubMed: 36933823]
37. Dooley DJ, Donovan CM, Meder WP & Whetzel SZ Preferential action of gabapentin and pregabalin at P/Q-type voltage-sensitive calcium channels: inhibition of K^+-evoked [^{3}H]-norepinephrine release from rat neocortical slices. Synapse 45, 171–190 (2002). [PubMed: 12112396]
38. Infield DT et al. Cation–π Interactions and their functional roles in membrane proteins. J. Mol. Biol. 433, 167035 (2021). [PubMed: 33957146]
39. Chen YH et al. Structural basis of the α1-β subunit interaction of voltage-gated Ca^{2+} channels. Nature 429, 675–680 (2004). [PubMed: 15170217]

40. Van Petegem F, Clark KA, Chatelain FC & Minor DL Jr. Structure of a complex between a voltage-gated calcium channel β-subunit and an α-subunit domain. Nature 429, 671–675 (2004). [PubMed: 15141227]
41. Van Petegem F, Duderstadt KE, Clark KA, Wang M & Minor DL Jr. Alanine-scanning mutagenesis defines a conserved energetic hotspot in the $Ca_V\alpha_1$ AID-$Ca_V\beta$ interaction site that is critical for channel modulation. Structure 16, 280–294 (2008). [PubMed: 18275819]
42. Bai L, You Q, Feng X, Kovach A & Li H Structure of the ER membrane complex, a transmembrane-domain insertase. Nature 584, 475–478 (2020). [PubMed: 32494008]
43. Wu J et al. Structure of the voltage-gated calcium channel $Ca_v1.1$ at 3.6 Å resolution. Nature 537, 191–196 (2016). [PubMed: 27580036]
44. Yao X, Gao S & Yan N Structural basis for pore blockade of human voltage-gated calcium channel $Ca_v1.3$ by motion sickness drug cinnarizine. Cell Res. 10.1038/s41422-022-00663-5 (2022).
45. Gao S, Yao X & Yan N Structure of human $Ca_v2.2$ channel blocked by the painkiller ziconotide. Nature 596, 143–147 (2021). [PubMed: 34234349]
46. Zhao Y et al. Cryo-EM structures of apo and antagonist-bound human $Ca_v3.1$. Nature 576, 492–497 (2019). [PubMed: 31766050]
47. Brown JP, Dissanayake VU, Briggs AR, Milic MR & Gee NS Isolation of the [^{3}H] gabapentin-binding protein/$\alpha_2\delta$ Ca^{2+} channel subunit from porcine brain: development of a radioligand binding assay for $\alpha_2\delta$ subunits using [^{3}H]leucine. Anal. Biochem. 255, 236–243 (1998). [PubMed: 9451509]
48. Dolphin AC Calcium channel auxiliary $\alpha_2\delta$ and beta subunits: trafficking and one step beyond. Nat. Rev. Neurosci. 13, 542–555 (2012). [PubMed: 22805911]
49. Wu J et al. Structure of the voltage-gated calcium channel $Ca_v1.1$ complex. Science 350, aad2395 (2015). [PubMed: 26680202]
50. Gumerov VM et al. Amino acid sensor conserved from bacteria to humans. Proc. Natl Acad. Sci. USA 119, e2110415119 (2022). [PubMed: 35238638]
51. Wang M, Offord J, Oxender DL & Su TZ Structural requirement of the calcium-channel subunit $\alpha_2\delta$ for gabapentin binding. Biochem. J. 342, 313–320 (1999). [PubMed: 10455017]
52. Zhao Y et al. Molecular basis for ligand modulation of a mammalian voltage-gated Ca^{2+} Channel. Cell 177, 1495–1506 (2019). [PubMed: 31150622]
53. He L et al. Structure, gating, and pharmacology of human $Ca_V3.3$ channel. Nat. Commun. 13, 2084 (2022). [PubMed: 35440630]
54. Gao S & Yan N Structural basis of the modulation of the voltage-gated calcium ion channel $Ca_v1.1$ by dihydropyridine compounds. Angew. Chem. Int. Ed. Engl. 60, 3131–3137 (2021). [PubMed: 33125829]
55. Tao X, Lee A, Limapichat W, Dougherty DA & MacKinnon R A gating charge transfer center in voltage sensors. Science 328, 67–73 (2010). [PubMed: 20360102]
56. Arrigoni C et al. Quaternary structure independent folding of voltage-gated ion channel pore domain subunits. Nat. Struct. Mol. Biol. 29, 537–548 (2022). [PubMed: 35655098]
57. Bourdin B, Briot J, Tetreault MP, Sauve R & Parent L Negatively charged residues in the first extracellular loop of the L-type $Ca_V1.2$ channel anchor the interaction with the $Ca_V\alpha2\delta1$ auxiliary subunit. J. Biol. Chem. 292, 17236–17249 (2017). [PubMed: 28864774]
58. Dahimene S et al. The $\alpha_2\delta$-like protein Cachd1 increases N-type calcium currents and cell surface expression and competes with $\alpha_2\delta$-1. Cell Rep. 25, 1610–1621 (2018). [PubMed: 30404013]
59. Canti C et al. The metal-ion-dependent adhesion site in the Von Willebrand factor-A domain of $\alpha_2\delta$ subunits is key to trafficking voltage-gated Ca^{2+} channels. Proc. Natl Acad. Sci. USA 102, 11230–11235 (2005). [PubMed: 16061813]
60. Gurnett CA, Felix R & Campbell KP Extracellular interaction of the voltage-dependent Ca^{2+} channel $\alpha_2\delta$ and α_1 subunits. J. Biol. Chem. 272, 18508–18512 (1997). [PubMed: 9218497]
61. Opatowsky Y, Chomsky-Hecht O, Kang MG, Campbell KP & Hirsch JA The voltage-dependent calcium channel β subunit contains two stable interacting domains. J. Biol. Chem. 278, 52323–52332 (2003). [PubMed: 14559910]

62. Altier C et al. The Cavβ subunit prevents RFP2-mediated ubiquitination and proteasomal degradation of L-type channels. Nat. Neurosci. 14, 173–180 (2011). [PubMed: 21186355]
63. Waithe D, Ferron L, Page KM, Chaggar K & Dolphin AC β-Subunits promote the expression of $Ca_V2.2$ channels by reducing their proteasomal degradation. J. Biol. Chem. 286, 9598–9611 (2011). [PubMed: 21233207]
64. Fang K & Colecraft HM Mechanism of auxiliary β-subunit-mediated membrane targeting of L-type ($Ca_V1.2$) channels. J. Physiol. 589, 4437–4455 (2011). [PubMed: 21746784]
65. Altier C et al. Trafficking of L-type calcium channels mediated by the postsynaptic scaffolding protein AKAP79. J. Biol. Chem. 277, 33598–33603 (2002). [PubMed: 12114507]
66. Obermair GJ et al. Reciprocal interactions regulate targeting of calcium channel beta subunits and membrane expression of α_1 subunits in cultured hippocampal neurons. J. Biol. Chem. 285, 5776–5791 (2010). [PubMed: 19996312]
67. Leroy J et al. Interaction via a key tryptophan in the I-II linker of N-type calcium channels is required for β1 but not for palmitoylated β2, implicating an additional binding site in the regulation of channel voltage-dependent properties. J. Neurosci. 25, 6984–6996 (2005). [PubMed: 16049174]
68. Pleiner T et al. A selectivity filter in the ER membrane protein complex limits protein misinsertion at the ER. J. Cell Biol. 222, e202212007 (2023). [PubMed: 37199759]
69. Opatowsky Y, Chen CC, Campbell KP & Hirsch JA Structural analysis of the voltage-dependent calcium channel β subunit functional core and its complex with the α1 interaction domain. Neuron 42, 387–399 (2004). [PubMed: 15134636]
70. Dolphin AC & Lee A Presynaptic calcium channels: specialized control of synaptic neurotransmitter release. Nat. Rev. Neurosci. 21, 213–229 (2020). [PubMed: 32161339]
71. Felix R, Gurnett CA, De Waard M & Campbell KP Dissection of functional domains of the voltage-dependent Ca^{2+} channel $\alpha_2\delta$ subunit. J. Neurosci. 17, 6884–6891 (1997). [PubMed: 9278523]
72. Smart OS, Neduvelil JG, Wang X, Wallace BA & Sansom MS HOLE: a program for the analysis of the pore dimensions of ion channel structural models. J. Mol. Graph. 14, 354–360 (1996). [PubMed: 9195488]
73. Pravda L et al. MOLEonline: a web-based tool for analyzing channels, tunnels and pores (2018 update). Nucleic Acids Res. 46, W368–W373 (2018). [PubMed: 29718451]
74. Schmidt TG & Skerra A The Strep-tag system for one-step purification and high-affinity detection or capturing of proteins. Nat. Protoc. 2, 1528–1535 (2007). [PubMed: 17571060]
75. Liao M, Cao E, Julius D & Cheng Y Structure of the TRPV1 ion channel determined by electron cryo-microscopy. Nature 504, 107–112 (2013). [PubMed: 24305160]
76. Elegheert J et al. Lentiviral transduction of mammalian cells for fast, scalable and high-level production of soluble and membrane proteins. Nat. Protoc. 13, 2991–3017 (2018). [PubMed: 30455477]
77. Goehring A et al. Screening and large-scale expression of membrane proteins in mammalian cells for structural studies. Nat. Protoc. 9, 2574–2585 (2014). [PubMed: 25299155]
78. Lee H, Lolicato M, Arrigoni C & Minor DL Jr. Production of K2P2.1 (TREK-1) for structural studies. Methods Enzymol. 653, 151–188 (2021). [PubMed: 34099170]
79. Shaya D et al. Voltage-gated sodium channel (NaV) protein dissection creates a set of functional pore-only proteins. Proc. Natl Acad. Sci. USA 108, 12313–12318 (2011). [PubMed: 21746903]
80. Abderemane-Ali F, Findeisen F, Rossen ND & Minor DL Jr. A selectivity filter gate controls voltage-gated calcium channel calcium-dependent inactivation. Neuron 101, 1134–1149 (2019). [PubMed: 30733149]
81. Findeisen F & Minor DL Jr. Disruption of the IS6-AID linker affects voltage-gated calcium channel inactivation and facilitation. J. Gen. Physiol. 133, 327–343 (2009). [PubMed: 19237593]
82. Hamill OP, Marty A, Neher E, Sakmann B & Sigworth FJ Improved patch-clamp techniques for high-resolution current recording from cells and cell-free membrane patches. Pflugers Arch. 391, 85–100 (1981). [PubMed: 6270629]
83. Mastronarde DN Automated electron microscope tomography using robust prediction of specimen movements. J. Struct. Biol. 152, 36–51 (2005). [PubMed: 16182563]

84. Punjani A, Rubinstein JL, Fleet DJ & Brubaker MA cryoSPARC: algorithms for rapid unsupervised cryo-EM structure determination. Nat. Methods 14, 290–296 (2017). [PubMed: 28165473]

85. Zivanov J et al. New tools for automated high-resolution cryo-EM structure determination in RELION-3. eLife 7, e42166 (2018). [PubMed: 30412051]

86. Liebschner D et al. Macromolecular structure determination using X-rays, neutrons and electrons: recent developments in Phenix. Acta Crystallogr. D 75, 861–877 (2019).

87. Kelley LA, Mezulis S, Yates CM, Wass MN & Sternberg MJ The Phyre2 web portal for protein modeling, prediction and analysis. Nat. Protoc. 10, 845–858 (2015). [PubMed: 25950237]

88. Emsley P, Lohkamp B, Scott WG & Cowtan K Features and development of Coot. Acta Crystallogr. D 66, 486–501 (2010). [PubMed: 20383002]

89. Moriarty NW, Grosse-Kunstleve RW & Adams PD Electronic Ligand Builder and Optimization Workbench (eLBOW): a tool for ligand coordinate and restraint generation. Acta Crystallogr. D 65, 1074–1080 (2009). [PubMed: 19770504]

90. Williams CJ et al. MolProbity: more and better reference data for improved all-atom structure validation. Protein Sci. 27, 293–315 (2018). [PubMed: 29067766]

91. Pettersen EF et al. UCSF ChimeraX: structure visualization for researchers, educators, and developers. Protein Sci. 30, 70–82 (2021). [PubMed: 32881101]

92. Wallace AC, Laskowski RA & Thornton JM LIGPLOT: a program to generate schematic diagrams of protein-ligand interactions. Protein Eng. 8, 127–134 (1995). [PubMed: 7630882]

93. Laskowski RA & Swindells MB LigPlot+: multiple ligand-protein interaction diagrams for drug discovery. J. Chem. Inf. Model. 51, 2778–2786 (2011). [PubMed: 21919503]

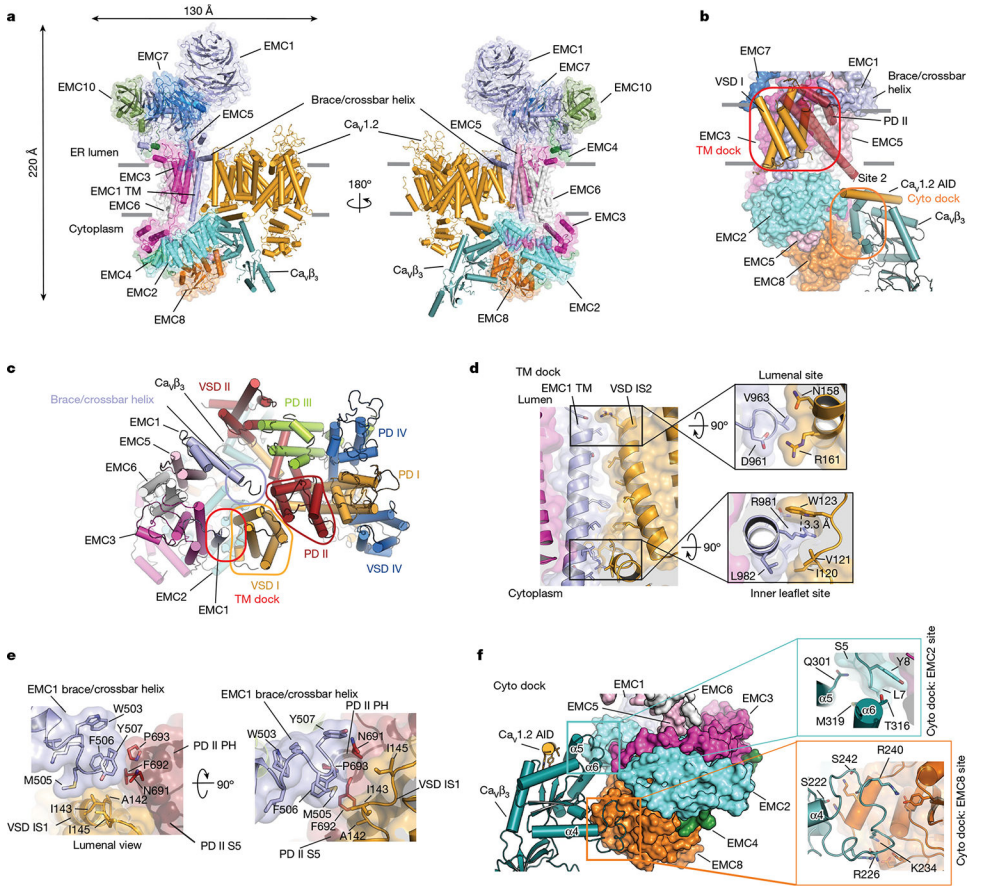

Fig. 1 |. The structure of the EMC–Ca$_V$1.2(ΔC)–Ca$_V$β$_3$ complex.

a, Cartoon structure side views of the EMC–Ca$_V$1.2(ΔC)–Ca$_V$β$_3$ complex. EMC1, EMC2, EMC3, EMC4, EMC5, EMC6, EMC7, EMC8, EMC10, CaV1.2 and Ca$_V$β$_3$ are shown. EMC subunits are shown with semi-transparent surfaces. The arrows indicate dimensions. **b**, The location of the TM dock and Cyto dock EMC client-binding sites. Ca$_V$1.2 components interacting with the EMC are shown as cylinders. The AID helix is also shown. The grey bars in **a** and **b** denote the membrane. **c**, Lumenal view of the EMC–Ca$_V$1.2(ΔC)–Ca$_V$β$_3$ complex transmembrane elements. EMC components are shown as cylinders. Ca$_V$1.2(ΔC) domains are coloured as domain I (yellow orange), domain II (dark red), domain III (lime) and domain IV (deep blue). VSD and PD elements are labelled. The red oval in **b** and **c** shows the TM dock site. The pale purple circle shows the site of interaction of the EMC1 brace/crossbar helix with Ca$_V$1.2 VSD I and PD II (outlined). **d**, Side view of the TM dock–VSD I interaction. Insets: details of interactions in the of the EMC1 brace/crossbar helix with Ca$_V$1.2 VSD I and PD II. **f**, Details of the Cyto dock. Ca$_V$β and AID helix are shown as cylinders. EMC2, EMC3, EMC4, EMC5, EMC6 and EMC8 are shown as surfaces. Insets: details of the EMC2 and EMC8 sites.

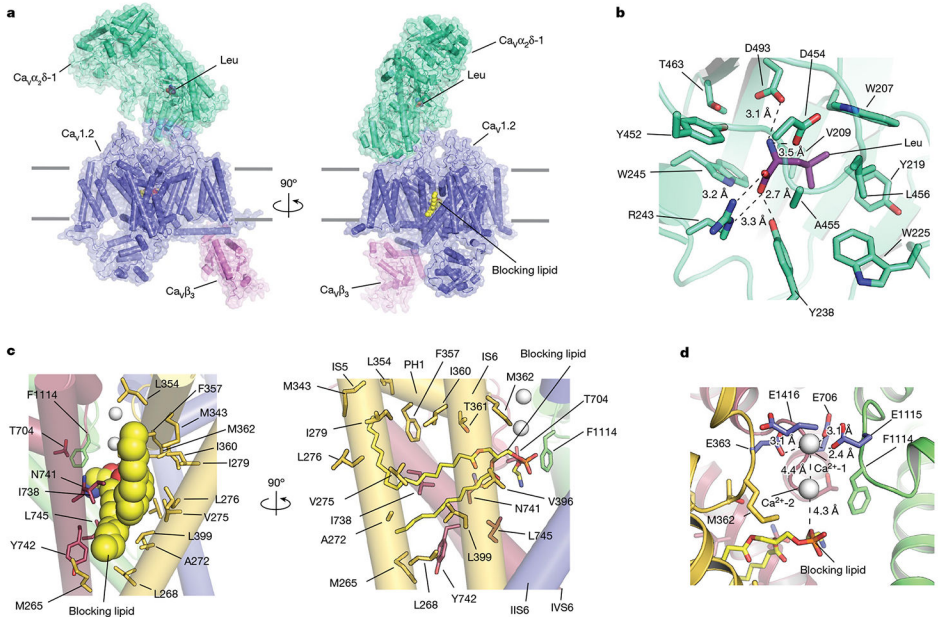

Fig. 2 |. The structure of the $Ca_V1.2(\Delta C)$–$Ca_V\beta_3$–$Ca_V\alpha_2\delta$-1 channel complex.

a, Side views of $Ca_V1.2(\Delta C)$–$Ca_V\beta_3$–$Ca_V\alpha_2\delta$-1. Leucine and blocking lipid are shown as space filling. The grey bars denote the membrane. **b**, Details of the $Ca_V\alpha_2\delta$-1 Cache1 ligand-binding site. Leucine (purple) and contacting side chains from $Ca_V\alpha_2\delta1$ (green cyan) are shown as sticks. **c**, Details of the blocking-lipid-binding site. $Ca_V1.2$ PDs are shown as cylinders and coloured as follows: PD I (yellow orange), PD II (dark red), PD III (lime) and PD IV (deep blue). Lipid-contact residues are shown as sticks. Blocking lipid is shown as space filling (left) and sticks (right). **d**, Interaction between the blocking lipid and SF ions. Hallmark SF calcium-binding residues are shown as sticks (purple). SF calcium ions are indicated.

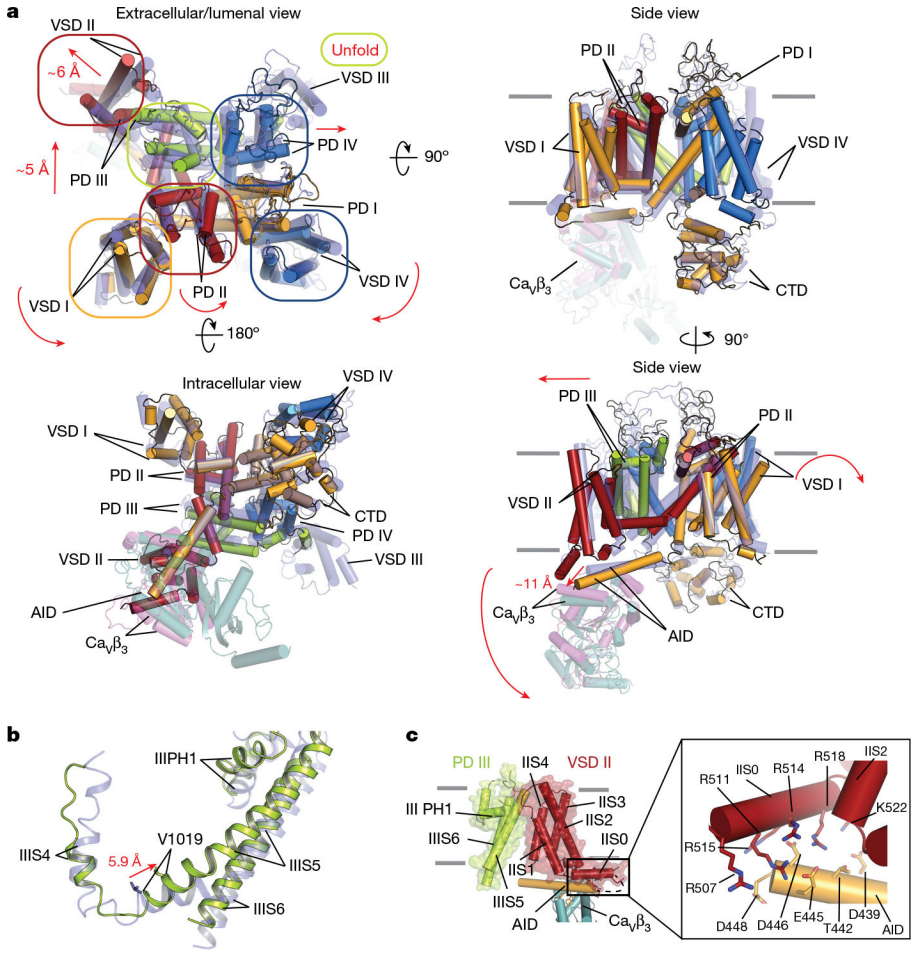

Fig. 3 |. EMC interactions remodel Ca_V structure and extract PD III.

a, Superposition of $Ca_V1.2$–$Ca_V\beta_3$ from the EMC and $Ca_V1.2(\Delta C)$–$Ca_V\beta_3$–$Ca_V\alpha_2\delta$-1 complexes. $Ca_V1.2$ elements from the EMC complex are coloured as follows: VSD I/PD I (yellow orange), VSD II/PD II (dark red), VSD III/PD III (lime) and VSD IV/PD IV (deep blue). $Ca_V1.2$ (purple) and $Ca_V\beta_3$ (magenta) from $Ca_V1.2(\Delta C)$–$Ca_V\beta_3$–$Ca_V\alpha_2\delta$ and $Ca_V\beta_3$ from the EMC (light teal) are semi-transparent. The red arrows indicate conformational changes between $Ca_V1.2(\Delta C)$–$Ca_V\beta_3$–$Ca_V\alpha_2\delta$-1 and EMC–$Ca_V1.2(\Delta C)$–$Ca_V\beta$. Coloured ovals highlight key domains reshaped by the EMC. **b**, Superposition of the S4 and S4–S5 linker–PD III elements from the EMC–$Ca_V1.2(\Delta C)$–$Ca_V\beta_3$ complex (lime) and $Ca_V1.2(\Delta C)$–$Ca_V\beta3$–$Ca_V\alpha_2\delta$-1 (purple). The Cα–Cα distance for Val1019 is indicated. **c**, Interactions within the $Ca_V\beta$–AID–VSD II–PD III subcomplex in EMC–$Ca_V1.2(\Delta C)$–$Ca_V\beta_3$. The grey bars in **a** and **c** denote the membrane.

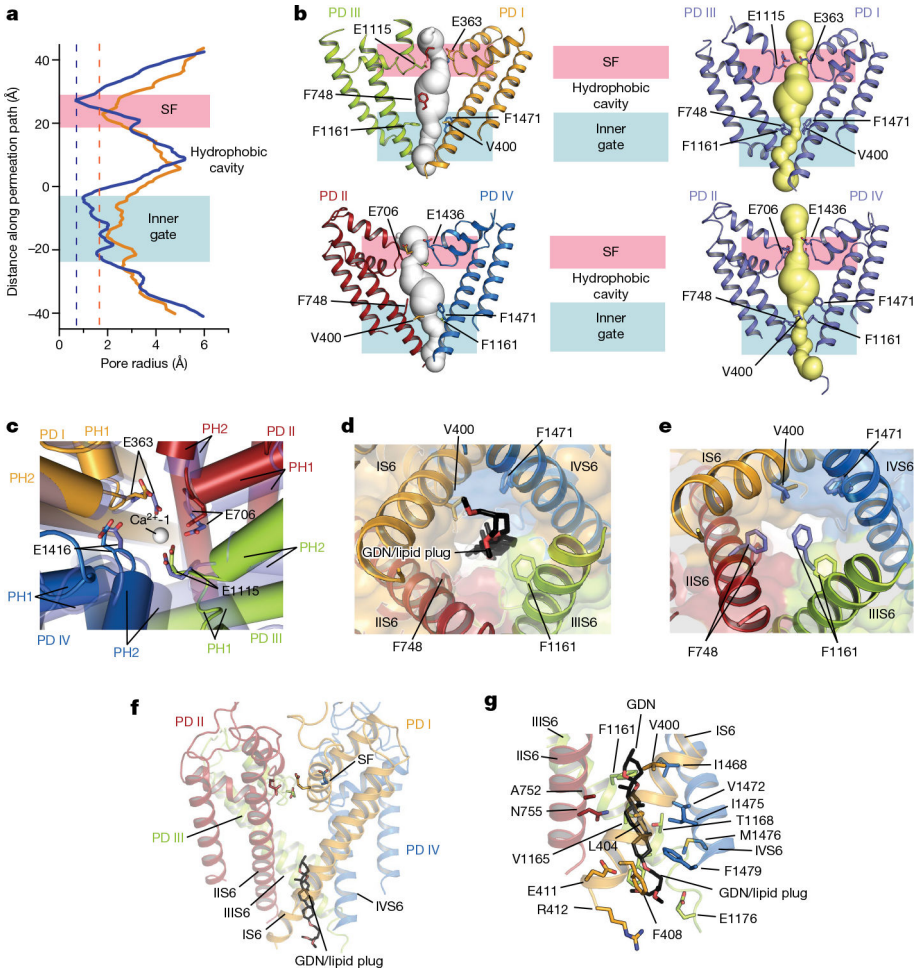

Fig. 4 |. EMC association causes $Ca_V1.2$ pore structural changes.

a, $Ca_V1.2$ pore profile comparison for EMC–$Ca_V1.2$(ΔC)–$Ca_V\beta_3$ (orange) and $Ca_V1.2$(ΔC)–$Ca_V\beta_3$–$Ca_V\alpha_2\delta$-1 (blue), calculated using HOLE[72]. EMC: SF = 1.78 Å, inner gate = 1.98 Å; $Ca_V1.2$: SF = 0.65 Å, inner gate = 0.98 Å. **b**, Side views of EMC–$Ca_V1.2$(ΔC)–$Ca_V\beta_3$ (left) and $Ca_V1.2$(ΔC)–$Ca_V\beta_3$–$Ca_V\alpha_2\delta$ (right) pore profiles calculated using MOLE[73]. The SF, central cavity and hydrophobic gate regions are indicated. SF and intracellular gate residues are shown. **c**, Comparison of the $Ca_V1.2$ SF filter regions in the EMC–$Ca_V1.2$(ΔC)–$Ca_V\beta_3$ pore (PD I, PD II, PD III and PD IV) and $Ca_V1.2$(ΔC)–$Ca_V\beta_3$–$Ca_V\alpha_2$ δ-1 (semi-transparent, purple). Ca^{2+}−1 from $Ca_V1.2$(ΔC)–$Ca_V\beta_3$–$Ca_V\alpha_2\delta$-1 is shown as a white sphere. **d**,**e**, View of the $Ca_V1.2$ intracellular gate from EMC–$Ca_V1.2$(ΔC)–$Ca_V\beta_3$ (**d**) and $Ca_V1.2$(ΔC)–$Ca_V\beta_3$–$Ca_V\alpha_2\delta$-1 (**e**). GDN is shown as sticks. PDs are coloured as follows: PD I (yellow orange), PD II (dark red), PD III (lime) and PD IV (deep blue). **f**,**g**, Side views of the EMC–$Ca_V1.2$(ΔC)–$Ca_V\beta_3$ pore showing global (**f**) and detailed (**g**) views. SF glutamates in **e** and GDN-contacting residues in **f** are shown as sticks. PD elements are labelled.

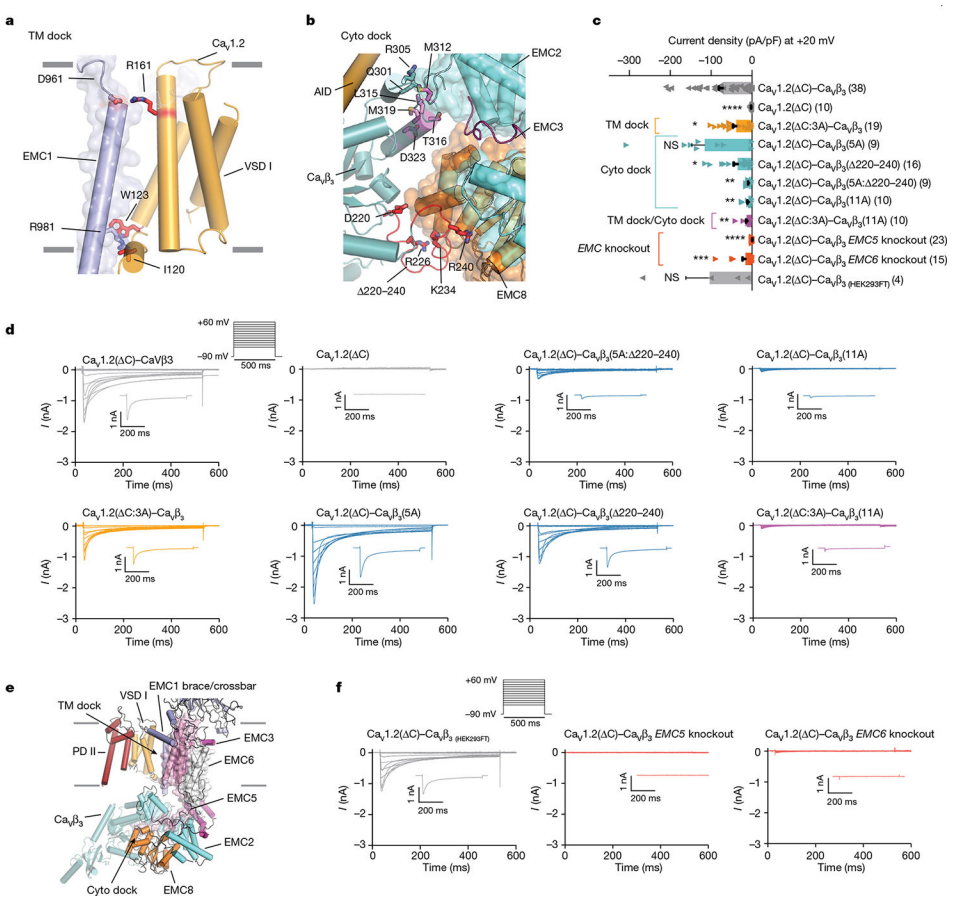

Fig. 5 |. Disruption of EMC–channel interactions affects Ca_V function.

a,**b**, Cartoon diagrams showing the location of TM dock 3A mutants (**a**), and Cyto dock 5A (magenta), Δ220–240 (red) and 11A (sticks) mutants (**b**). **c**, Current densities at +20 mV for the indicated channels and HEK293FT cell lines. Data are mean ± s.e.m. The values in parentheses indicate *n* independent cells examined over ≥2 independent experiments. Statistical significance was assessed using two-sided unpaired *t*-tests between $Ca_V1.2$(ΔC)–$Ca_V\beta_3$ and mutants. ****$P < 0.0001$, ***$P < 0.001$, **$P < 0.01$, *$P = 0.01$–0.05; NS, $P > 0.05$. **d**, Exemplar Ca^{2+} currents for HEK293 cells expressing the indicated channels in the presence of $Ca_V\alpha_2\delta$-1. Insets: the stimulation protocol and currents at +20 mV. **e**, Cartoon of the EMC–$Ca_V1.2$(ΔC)–$Ca_V\beta_3$ complex showing the following selected elements: EMC1, EMC2, EMC3, EMC5, EMC6, EMC8, $Ca_V1.2$ VSD I and PD II, and $Ca_V\beta_3$. The arrows indicate the TM dock and Cyto dock. Surfaces are shown for EMC5 and EMC6. **f**, Exemplar $Ca_V1.2$(ΔC)–$Ca_V\beta_3$–$Ca_V\alpha_2\delta$-1 Ca^{2+} currents for HEK293FT and HEK293FT *EMC5*-knockout and *EMC6*-knockout cells. Insets: the protocol and currents at +20 mV.